การศึกษาสมบัติทางไฟฟ้าเชิงทฤษฎีของเมทิลแอมโมเนียมลีดไอโอไดด์เพอรอฟสไกต์ภายใต้ความดันสูง

นางสาววิชวรรณ สกุลสุพิชญ์

วิทยานิพนธ์นี้เป็นส่วนหนึ่งของการศึกษาตามหลักสูตรปริญญาวิทยาศาสตรมหาบัณฑิต
สาขาวิชาฟิสิกส์ภาควิชาฟิสิกส์
คณะวิทยาศาสตร์ จุฬาลงกรณ์มหาวิทยาลัย
ปีการศึกษา 2559

THEORETICAL STUDIES OF ELECTRONIC PROPERTIES OF METHYLAMMONIUM LEAD IODIDE PEROVSKITE UNDER HIGH PRESSURE

Miss Vichawan Sakulsupich

A Thesis Submitted in Partial Fulfillment of the Requirements

for the Degree of Master of Science Program in Physics

Department of Physics

Faculty of Science

Chulalongkorn University

Academic Year 2016

Thesis Title	THEORETICAL STUDIES OF ELECTRONIC PROPERTIES OF METHYLAMMONIUM LEAD IODIDE PEROVSKITE UNDER HIGH PRESSURE
By	Miss Vichawan Sakulsupich
Field of Study	Physics
Thesis Advisor	Associate Professor Thiti Bovornratanaraks, Ph.D.

Accepted by the Faculty of Science, Chulalongkorn University in Partial Fulfillment of the Requirements for the Master's Degree

..... Dean of the Faculty of Science
(Associate Professor Polkit Sangvani, Ph.D.)

THESIS COMMITTEE

..... Chairman
(Assistant Professor Rattachat Mongkolnavin, Ph.D.)

..... Thesis Advisor
(Associate Professor Thiti Bovornratanaraks, Ph.D.)

..... Examiner
(Assistant Professor Nuttakorn Thubthong, Ph.D.)

..... External Examiner
(Assistant Professor Supab Choopun, Ph.D.)

วิชวรรณ สกุลสุพิชญ์ : การศึกษาสมบัติทางไฟฟ้าเชิงทฤษฎีของเมทิลแอมโมเนียมลีดไอโอไดด์เพอรอฟสไกต์ภายใต้ความดันสูง (Theoretical Studies of Electronic Properties of Methylammonium Lead Iodide Perovskite under High Pressure) อ.ที่ปรึกษาวิทยานิพนธ์หลัก: รศ. ดร. ธิติ บวรรัตนารักษ์,95 หน้า.

เซลล์ไฟฟ้าจากแสงอาทิตย์นับเป็นทางเลือกที่สะอาดและยั่งยืนทางเลือกหนึ่ง การค้นคว้าวิจัยเพื่อพัฒนาเซลล์ไฟฟ้าแสงอาทิตย์ที่มีต้นทุนการผลิตต่ำและประสิทธิภาพสูงจึงก้าวหน้าไปอย่างรวดเร็ว ในช่วงสิบปีที่ผ่านมามีการนำสารกึ่งตัวนำประเภทไฮบริดออร์แกนิก-อินออร์แกนิกเพอรอฟสไกต์มาเป็นส่วนประกอบหลักในเซลล์ไฟฟ้าแสงอาทิตย์ สารชนิดนี้มีจุดเด่นในด้านต้นทุนในการสังเคราะห์ที่ต่ำ สังเคราะห์ได้ง่าย และเมื่อนำมาประกอบเป็นเซลล์ไฟฟ้าแสงอาทิตย์แล้วมีประสิทธิภาพการแปลงพลังงานแสงอาทิตย์เป็นพลังงานไฟฟ้าสูง แต่สารกึ่งตัวนำดังกล่าวมีข้อด้อยที่ไม่อาจมองข้ามได้อยู่ กล่าวคือ นักวิทยาศาสตร์พบว่าเพอรอฟสไกต์มีความคงทนต่ำ ไม่สามารถคงสถานะไว้ได้ในสิ่งแวดล้อมที่ชื้น มีออกซิเจน และยังสลายตัวเร็วขึ้นเมื่อมีแสงในย่านอัลตราไวโอเลตตกกระทบ ทำให้แม้จะสังเคราะห์ได้ในต้นทุนต่ำ แต่ก็ยังไม่สามารถนำมาผลิตใช้ในเชิงธุรกิจได้ เพื่อหาสาเหตุของการสูญเสียเสถียรภาพภายใต้อุณหภูมิ ผู้เขียนจึงศึกษาสมบัติทางโครงสร้างเชิงทฤษฎีของสารสารกึ่งตัวนำประเภทไฮบริดออร์แกนิก-อินออร์แกนิกเพอรอฟสไกต์ที่มีองค์ประกอททางเคมี คือ เมทิลแอมโมเนียมลีดไอโอไดด์เพอรอฟสไกต์ ซึ่งเป็นสารชนิดหลักที่ใช้ในงานทดลอง ศึกษาโดยใช้แบบจำลองทางทฤษฎีฟังก์ชันนอลของความหนาแน่น เพื่อศึกษาความสัมพันธ์ระหว่างพลวัฒน์ในระบบที่เกิดจากการหมุนของโมเลกุลเมทิลแอมโมเนียมกับสมบัติเชิงโครงสร้างของวัสดุ ในงานนี้ผู้เขียนกล่าวถึงความสำคัญของการเพิ่มพารามิเตอร์อันตรกิริยาแวนเดอวาลส์ต่อความแม่นยำของการคำนวณ และศึกษาสมบัติเชิงโครงสร้างและทางไฟฟ้าของเมทิลแอมโมเนียมลีดไอโอไดด์เพอรอฟสไกต์ภายความดันสูง พบว่าเมื่อให้ความดันเมทิลแอมโมเนียมลีดไอโอไดด์เพอรอฟสไกต์มีการมีค่าช่องว่างระหว่างพลังงาน (Energy Band) ต่างจากที่ความดันปกติ ซึ่งแป็นการชี้นำว่าการใช้ความดันเป็นปัจจัยเพื่อควบคุมค่าช่องว่างระว่างพลังงานในสารกึ่งตัวนำชนิดนี้ได้

ภาควิชา ฟิสิกส์ ลายมือชื่อนิสิต .....

สาขาวิชา ฟิสิกส์ ลายมือชื่อ อ.ที่ปรึกษาหลัก .....

ปีการศึกษา 2559

5772147523: MAJOR PHYSICS
KEYWORDS: PEROVSKITE / DENSITY FUNCTIONAL THEORY

VICHAWAN SAKULSUPICH : THEORETICAL STUDIES OF ELECTRONIC PROPERTIES OF METHYLAMMONIUM LEAD IODIDE PEROVSKITE UNDER HIGH PRESSURE. ADVISOR : Assoc. Prof. Thiti Bovornratanaraks, Ph.D., 95 pp.

Many researchers have claimed that hybrid organic−inorganic perovskite (HOIP) could hold the key to the new era of photovoltaic technology, owing to its efficiency, both energetically and economically. Despite all its merits, perovskite solar cell is plagued by an indispensable draw back; it degrades precipitously under sunlight. Not only sunlight that has destructive effects on perovskites, humidity and high temperature also cause the compound to disintegrate. In this work, we present a review on structural properties of the archetypal perovskite, the methylammonium lead iodide perovskite, as reported by various experiments. We performed density functional theory calculations to study the role of methylammonium dynamics to the structural properties. We also cover the most up-to-date reports on pressurization experiments. The effects of pressure on the material structural and electronic properties is also discussed.

Department : Physics Student's Signature .....
Field of Study : Physics Advisor's Signature .....
Academic Year : 2016

Acknowledgements

While shaping this thesis, I, the author, was also being shaped into a more solid human. I believe that behind any scientific discoveries, even in physical science, the hearts and altruism of many other great people were involved. Likewise, the journey I took while composing this thesis would not be a whole without these great people I met along the way.

I would like to express my sincere gratitude to my dear advisor, Assoc. Prof. Thiti Bovornratanaraks, who has been with me from the start to the end. It was his words that inspired this work, and his patience and sympathetic gestures that kept me in one piece through the lows.

I am also grateful for having Asst. Prof. Rattachat Mongkolnavin, Asst. Prof. Nuttakorn Thubthong and Asst. Prof. Supab Choopun as thesis committees. Their insightful commentary had made this thesis more completed.

For many years, I have been a part of Extreme Condition Physics Research Laboratory (ECPRL), I have always been thankful for the support from its members, especially Assoc. Prof. Udomsilp Pinsook for clarification on theoretical aspects. Much of the discussions we shared had given me inspirations. There are also Mr. Teerachote Pakornchote and Mr. Rakchat Klinkla whom I wish to express my gratitude to for their dedication on polishing the published article. The family-like, friendly atmosphere made asking for help much more comfortable. They are the oasis that I know will always be there.

This work is supported by Development and Promotion of Science and Technology Talents Project (DPST) scholarship, 90^{th} Anniversary of Chulalongkorn University Scholarship. The computation resources were provided by NECTEC's eScience Consortium, National Astronomical Research Institute of Thailand (NARIT) Chalawan Clusters and ECPRL clusters.

It was a long journey of discovering novel science and uncovering the truer self, believe it or not.

Contents

Chapter Page

List of Tables

List of Figures

Figure Page

CHAPTER I

INTRODUCTION

The industrialization began when human make use of fossil fuel. Several decades later, we realized that fossil fuel, our main source of energy, is not only limited in quantity, but also pollute the environment. We are in need of alternative energy sources, ones that are both 'renewable' and 'clean'. When we consider the Earth as a closed system, its main energy source came from the Sun, which emits limitless energy, at least in the timespan of living things. However human, unlike plants, do not have innate ability to harvest the energy from sunlight. Thus, methods to convert sunlight into manageable energy, i.e. solar-cell technology, is crucial for advancement of humankind.

While sunlight has no monetary cost, the solar cell itself costs a fortune. For these reasons, researches on cost-efficient and safe solar cells has gained momentum over time. Silicon-based photovoltaic devices, which have the semiconductor silicon as the main constituent, are the most common commercialized types of solar cell panels. However, they are still expensive to process, their manufacturing procedures leave toxic by-products and are complicated to install.

The situation has drastically changed since researchers discovered that perovskites have the potential to be developed into cheap photovoltaics. Perovskites are a class of crystalline solid that generally have ABX_3 chemical formula, with BX_6 ions forming octahedral-shaped ions building blocks and A cation filled between the interstitial sites.[3] The octahedra are linked to each other at apexes, forming bulk solid. While both natural and synthetic solids may adopts perovskite crystal structure, specific combinations of ions leads to material that has promising properties. Hybrid organic-inorganic perovskites (HOIPs hereafter) consist of organic cations, usually methylammonium or formadinium, and inorganic parts, thus the name HOIP.

Perovskite-based solar cells have emerged as a promising technology for highly efficient and low-cost photovoltaics. Back in in 2006, the first report on perovskite solar cell gives only 2.2%. As more research interest goes into developing this material, the highest

efficiency reported so far goes beyond 20% [4]. This unprecedented rise in efficiency, with the added advantage of low-cost processing, made perovskite solar cells an exciting field of study. As such, many experts deemed this material class as game-changers that could revolutionize the industry into higher level. [5]

However, many challenges are still waiting to be resolved before the commercialization of perovskite solar cell could take place. [6] One major problem is that perovskites are highly unstable. They are sensitive to moisture, ultraviolet light and thermal stress. [7, 8, 9] The lifespan of most perovskite solar cells are in the order of weeks to only several months. [10], Even the most stable cell reported is guaranteed to last for one year under controlled conditions [11], whereas the well-established silicon solar cells would still be functioning fine for at least 25 years outdoors.

To tackle the instability of perovskite solar cell, various approaches and suggestions have been made by both experimentalists and theorists. Making finer film quality lessen the effect of moisture and air on the cell, as water and ionic defects travels through gaps between the grain [12]. Perovskite films can also be sealed off to minimize the damage from reaction with humidity and air. Such cell encapsulation has been demonstrated to slow done cell degradation.[13] Even better, coatings that incorporate luminescent photopolymers also have the capability to convert UV light, which is harmful to perovskites, into light in visible range[14]. These avoidance measures cannot be employed to solve problems from thermal stress since it cannot be 'avoided'. Thermal energy induces atoms to vibrate, and even small differences in atom arrangement affect stability. Perovskite have chemical formula ABX3, where A is an organic (or inorganic) cation, B is a metal atom and X is a halide. Theorists have suggested that the sensitivity to heat might be due to the dynamics of the organic constituent of the perovskite itself. To reduce these movement, perovskites are doped with metal cations. Introducing inorganic ions to A cite have shown to increase stability from less than 100 hours to beyond 1,000 hours [15]. Other methods to improve stability includes doping more than one type of cations, and changing the atom type of B and X [16]. Altering crystal structure may not result in positive effects. Fixing one problem affects everything else, for instance, cell may have improved lifespan at the expense of conversion efficiency.

Damage caused by thermal stress is hindering the advancement of perovskite solar cells. We only know that perovskites disintegrate under high temperature, but underlying cause of instability is still not well-established.[17] We believe that fundamental understanding of the cell complex dynamics will lead to suggestion on how to improve the cell. To do so, ab initio simulations is used.

Aside from improving stability, there are researches that focus on improving band gap [18, 19], i.e. the electronic property, in order to raise energy conversion efficiency, so that it approaches that of the theoretical QS limit. Doping metals not only have effect on structural property of perovskite, but also affect its electronic properties[10]. Thus the effect of doping is not straightforward.

In operation, the perovskite layer is coupled between other layers of materials, and there would be lattice mismatch causing strain in the material [20]. Effect of pressure to HOIPs have been studied experimentally, but not theoretically in-depth [21, 2]. This problem will also be investigated in this thesis.

1.1 Rationale and Assumption

In this study, only the archetypal HOIP, the methylammonium lead iodide ($MAPbI_3$ hereafter) perovskite will be investigated. We assume that the result could be extrapolated to explain other perovskite that have similar atomic combination. Our study focus on ambient temperature phases, at ambient and high pressure.

- At ambient pressure
  - We assume that the system is quasi-static and would assume lowest energy atomic configuration.
  - We assume that van der Waals force contributes to structural property of this structure, the spin-orbit coupling is neglected in ambient pressure calculations, as suggested by other literatures.

- At high pressure
  - There are observation on phase transition of $MAPbI_3$ at high pressure and there is electronic property change along the pressure increment.[2] The cause of changes in electronic property is still unknown.
  - Our assumption is that DFT could be employed to explain the phenomena.

1.2 Motivation

In this work, we mainly study the reorientation of MA cation in cubic $MAPbI_3$ perovskite and discussed the hydrogen bonding between the organic molecule and the inorganic octahedron cage at a given C-N axis direction. We focus on equilibrium structural configurations when methyl and ammonium groups are coherently rotated around C-N axis of MA cation.

This research is composed of consecutive parts. The first part concerning the role different exchange-correlation functional to the accuracy of calculation. Calculation accuracy will be analyzed by comparing this work's results to those of other research groups' and to published experimental data. The following part of research will be focused on the role of pressure to $MAPbI_3$ perovskites.

1. To examine the importance and accuracy of van der Waals interaction in MAPbI3 perovskite simulation in DFT calculation.
2. To examine the effect of methylammonium ion dynamics to the structural stability of $MAPbI_3$ perovskite systems
3. To study effect of pressure on the electronic properties and structure of $MAPbI_3$ perovskite systems

1.3 Summary of Contribution

- This study will focus on $MAPbI_3$ perovskites in their cubic structure which is the phase occurring at room temperature and atmospheric pressure.
- Density functional theory will be used as primary tool in this research.

- The effect of different pseudopotentials and interaction included in calculation will be explored in detail.
- The importance of van der Waals interaction will be examined. This work will rationalize the physical importance of van der Waals interaction to $MAPbI_3$ perovskite systems.
- The interplay between the organic cation orientation and structural and electronic properties will be observed.
- Effects of pressure on electronic properties will also be investigated to establish a novel explanation of the interplay between MA ion orientation and structural and electronic properties.
- The final expected result is to bring into light the effect of dynamics and pressure to HOIPs electronic properties.

1.4 Thesis Organization

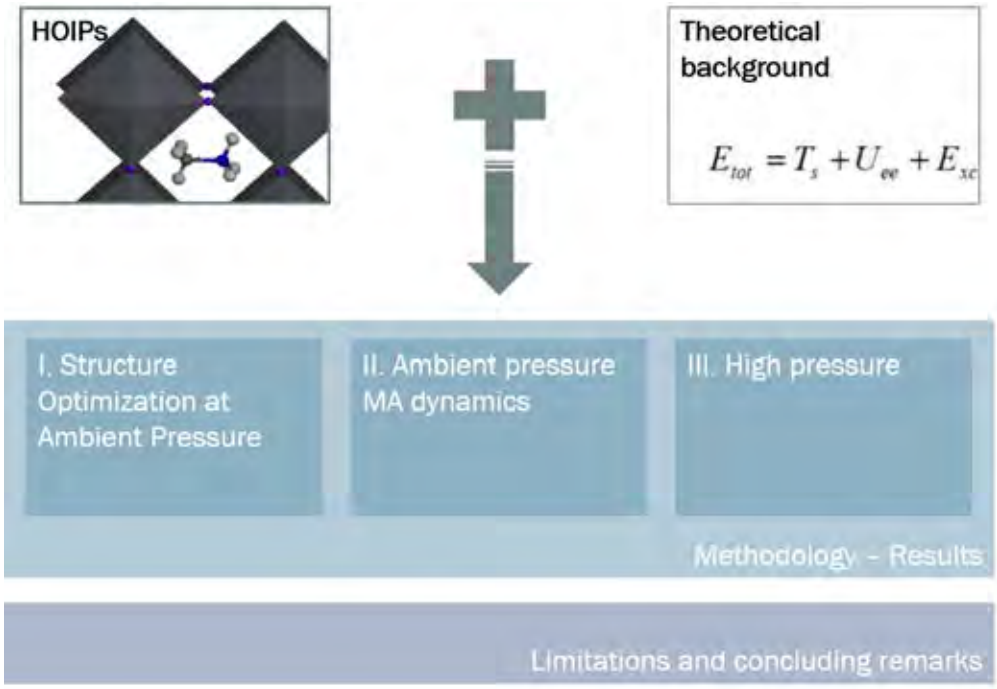

Figure 1.1: Graphical summary of this research.

This book of thesis is organized as follows. This Chapter I scopes the outline of the problem, which is then followed by Chapter II and Chapter III. Chapter II will give background on crystal structure, perovskite structure, and how to classify them. Chapter III focuses mainly on theoretical aspects of the simulation. Chapter II and III may be read in any order, as the contents are not related, but insights from both chapter are required to fully understand the remaining of this work.

Chapter IV is about structural optimization of $MAPbI_3$ at ambient pressure. In this chapter, we evaluate the accuracy of various pseudopotentials. The goal is to opt for the most suitable pseudopotentials for $MAPbI_3$ system, the result from this chapter will become the standard of calculations of the following chapters. Chapter V is on the effect of methylammonium dynamics to structural property. Chapter VI main focus is on the electronic properties of $MAPbI_3$ at high pressure. The readers may skip Chapter V as minimal results from chapter V will be taken into the context of Chapter VI. Finally, Chapter VII summarizes this thesis, gives detailed limitations and suggests future works. A graphical organization of this thesis is shown in Fig.1.1.

CHAPTER II

PRELIMINARIES AND RELATED WORKS

In this chapter, we review related literatures on perovskite as photovoltaic material and their shortcomings. We also cover structural and electronic properties of all phases. Finally works on $MAPbI_3$ band gap engineering are also summarized. Related theoretical background is covered in a separated chapter, Chapter III.

2.1 Preliminaries

2.1.1 Crystal Structure

In the atomic scale, ideal crystalline solids consist of infinitely repeating identical sub-units, called 'unit cells'. In the same way as how repeating units of identical 'bricks' becomes a 'wall'. One form of unit cells is a three dimensional parallelepiped which may have unequal edge lengths, a, b, and c, and internal angles between the edges, α, β, and γ.

The unit cell consists of two parts: the lattice and the basis. A lattice is the 'shape' of the cell, denoted by lattice parameters, a, b, c, α, β, and γ. A lattice may have more than one lattice point, which is the point where atoms are placed. The basis may be viewed as positions of atoms relative to lattice points in a unit cell. A schematic model of unit cell is shown in Fig. 2.1

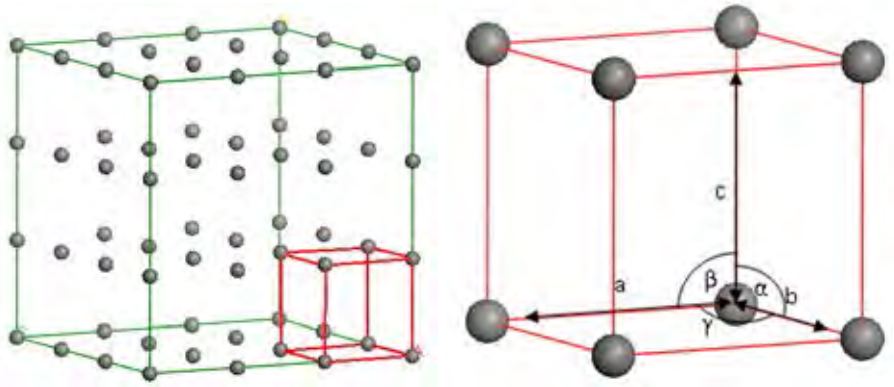

Figure 2.1: A model of crystalline solid along with a definition of lattice parameters

Since atoms in a unit cell are representable using mathematical symmetry operations, e.g. mirror planes, inversion points, and symmetry axis of rotation. It is conventional to describe the unit cell using groups of symmetry operations, or the 'space groups'. All possible two- and three-dimensional space groups are illustrated in the International Tables for Crystallography: Volume A. [22]

2.1.2 High Pressure Experiments

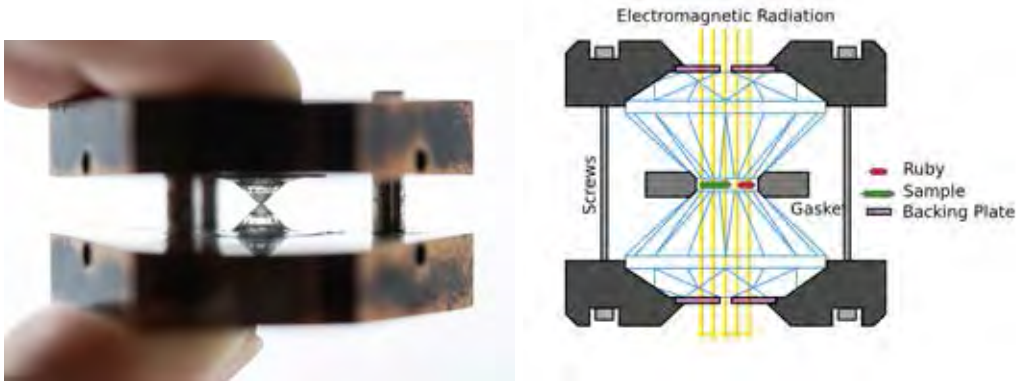

Figure 2.2: (Left) A diamond anvil cell without a gasket. (Right) A schematic diagram of a DAC.

High pressure physics is the study of properties of materials at extreme pressure. One way to conduct the experiment is by using diamond anvil cells (DACs). A DAC is composed of two diamonds, both diamonds have their culets (the pointy tips of a diamond) slightly cut off to have a small flat area. A sheet of metal, usually beryllium, tungsten, stainless steels or other simple-structure metal sheet is drilled through to form a small pinhole of matching dimension of the cut diamond culets. This metal sheet is call a gasket. The diamonds are arranged so that the culets face each other and the gasket is placed in between the metal, forming a closed pressure chamber. Samples are loaded into the chamber along with pieces of powdered ruby to measure the *in situ* pressure. All these instruments are then secured with bolts and screws. Pressure modulation is then done by carefully tightening the screws. A picture of a DAC is shown in Fig.2.2, diagram was taken from [23].

The diamond and gasket form a closed system. When the the screws of the DAC are tightened, the two diamonds move closer, making the volume of chamber shrinks and the pressure rises. Physical properties of the pressurized sample can be measured using different wavelengths electromagnetic radiation. Possible measurement include the structural properties from x-ray diffraction, optical band-gap using visible and infrared light sources. Real image of sample can also be photographed through an optical microscope.

2.2 Phase Transition of $MAPbI_3$

In this section, we review, first, the reported phase transition of $MAPbI_3$ at atmospheric pressure. Then, we cover recent reports on phase transitions occurs at higher pressure at ambient temperature.

2.2.1 $MAPbI_3$ Phases at Atmospheric Pressure

Both experiments and simulations suggest that $MAPbI_3$ exists in three phases at atmospheric pressure. At high temperature, it adopts cubic structure with space group $Pm\bar{3}m$. It undergoes first-order phase transition into tetragonal structure with space group $I4/mcm$ as the temperature lowers. Finally, as the temperature goes lower than ~ 160 K, it morphs into orthorhombic structure, with space group $Pnma$. The reported transition temperature are summarized in table 2.1.

Phase III $\rightarrow$ Phase II	Phase II $\rightarrow$ Phase I	Reference
165 K	327 K	[24]
161.4 K	330.4 K	[25]

Table 2.1: Phase transition temperature of $MAPbI_3$ at atmospheric pressure

Different phases of $MAPbI_3$ have differing octahedral orientation and MA dynamics. Cubic phase, or phase I, which exists at highest temperature, has the most ordered octahedral orientation. The octahedral network in this phase undergoes no tilting and can be described by Glazer's notation as $a^0a^0a^0$, symbolizing no tilt about any pseudocubic axes. [3] However the MA molecules in this phase bear highest kinetic energy and do not stay in static position. Various experiment techniques were employed to determine the exact position of these molecules but the attempts were futile. The only conclusion that can be drawn is that MA molecules are highly dynamic, the molecules seem to not have any preferred orientation nor form permanent grain boundaries. The space group

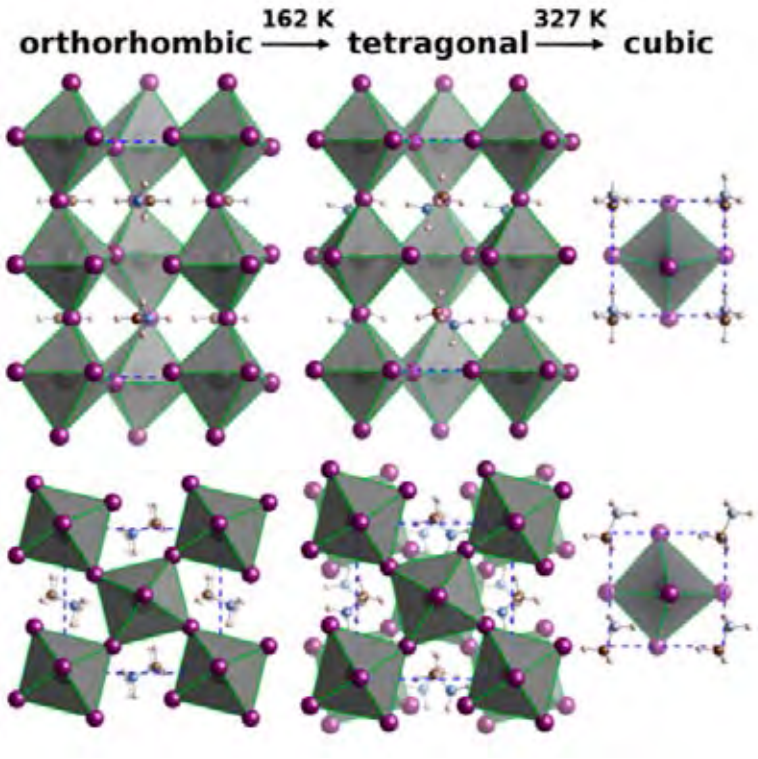

Figure 2.3: $MAPbI_3$ structures at atmospheric pressure. Figure taken from [1] with permission.

assigned to this phase, $Pm\bar{3}m$, only describe the orientation of Pb and I atoms, neglecting the disorder of MA orientation entirely. Cubic phase I's unit cell contains one formula unit of $MAPbI_3$.

When cubic phase I has its temperature lowered, it undergoes structural phase transition into tetragonal phase II. The octahedral network is slightly tilted in the lattice c axis. The tilting is $a^0a^0c^-$ in Glazer's notation. It identifies the tilting in c axis only. The tilted octahedra network, along with shortened Pb-I bond length made the interstitial site shrinks and thus the degree of freedom of MA is partially limited. In this tetragonal phase, the MA molecule have several preferred orientation, as confirmed by both experiment and simulation. See Fig 2.3 for the illustrated octahedral tilting. Due to the tilting, two formula units per unit cell is needed to describe the structure.

	Phase III	Phase II	Phase I
Structure	Orthorhombic	Tetragonal	Cubic
Space Group	$Pnma$	$I4/mcm$	$Pm\bar{3}m$
Z (Formula units)	4	2	1
Octahedral Tilting	$a^-b^-c^+$	$a^0a^0c^-$	$a^0a^0a^0$
MA orientation	Fixed	have preferred orientation	disordered

Table 2.2: Summary of structural properties of $MAPbI_3$ phases at atmospheric pressure

The orthorhombic phase III, which exists at low temperature, has the most tilted octahedral. The tilting occurs in all pseudocubic axes unequally, as denoted by $a^-b^-c^+$ in Glazer's notation. Since it has unequal tilting in all axes, four formula unit per unit cell is needed to fully describe the structure. For the low kinetic energy and small interstitial sites, the MA molecules have fixed orientation, with no dynamics, opposed to the previous two higher-temperature phases.

It is noteworthy that the trend of MA disorder, which increase with higher temperature, is in inverse trend of the degree of octahedron tilting. The observed octahedral tilting that in lower temperature phase III is not observed in high temperature phase I. This might be due to the limitation of both the x-ray and neutron diffraction experiment resolving power, and the nature of the measurement that give average position, rather than the exact position of each specific atom at specific spatial location. The aforementioned description of atmospheric pressure phases are summarized in Table 2.2.

2.2.2 Experiments on $MAPbI_3$ at High Pressure

Szafrański and Katrusiak reported high-pressure phase transition of $MAPbI_3$ at ambient temperature.[2] They pressurized single crystal $MAPbI_3$ using a DAC and measure x-ray diffraction and absorption edges as a function of pressure.

They reported that $MAPbI_3$ adopts tetragonal structure, i.e. Phase II, at atmospheric pressure, which is consistent with previous studies. [24, 25] Then the samples were loaded into a DAC and pressurized. X-ray diffraction shown that Phase II $MAPbI_3$ undergo structural phase transition at 0.3 GPa. The new phase was solved to be in $Im\bar{3}$ space group and is called Phase IV of $MAPbI_3$. Discontinuous cell volume drop indicates the phase transition. Phase IV is stable to about 2.5−2.7 GPa. Another volume drop marks a subsequent transition to phase V around 3.5 GPa, see Fig.2.4a. Both Phase IV

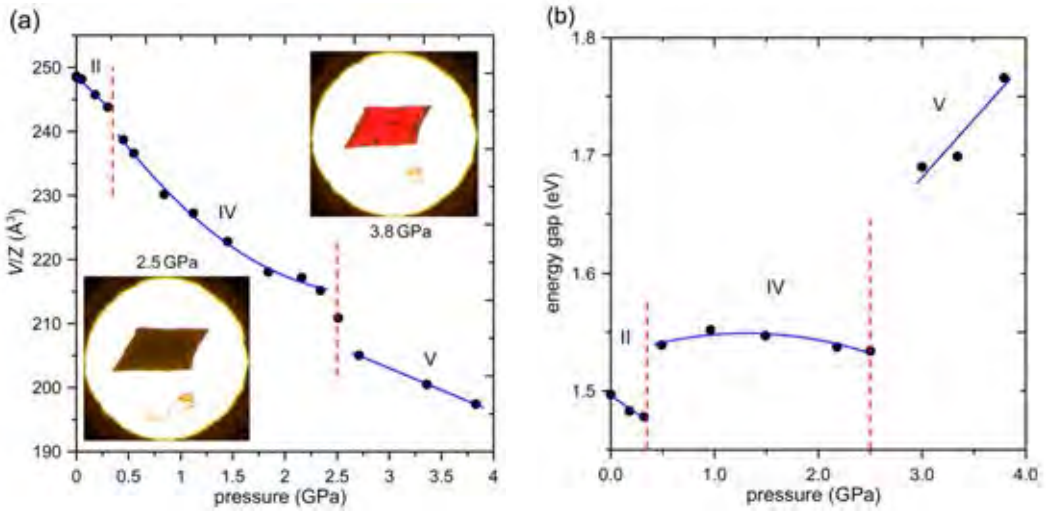

(a) $MAPbI_3$ volume plot

(b) $MAPbI_3$ energy gap plot

Figure 2.4: (a)Volume and (b) energy gap as a function of pressure. Figures taken from [2] with permission.

and Phase V contains 8 formula units of $MAPbI_3$ per unit cell and the octahedral tilting according to Glazer's notation is $a^+a^+a^+$, symbolizing equal tilting about all pseudocubic axes.

Physical properties changes were detected between the transition. Aside from aforementioned stepwise drop in cell volume, discontinuous change in energy gap is also present, as shown in Fig.2.4b. However, Szafrański and Katrusiak reported that both phase IV and V adopt the same space group. They had identified the space group by neglecting the MA orientation since carbon, nitrogen and hydrogen are undetectable by x-ray diffraction.

2.3 Interplay between Electronic and Structural Properties of $MAPbI_3$ Perovskite

2.3.1 The Study of Perovskite as Photovoltaic Material

Light shone upon peroveskites has never been brighter. The booming interest in hybrid organic–inorganic perovskites (HOIPs) originates from their potential applications in optoelectronic, thermoelectric, and photovoltaic technologies, owing to their favorable electronic, exitonic and optical properties. [26, 27, 28, 29] In only ten years' time, reported power conversion efficiencies of perovskite solar cells have risen from the first record of

4% in 2009, to 22.1% in 2016. [30, 27, 31] Intensive researches have rendered perovskite solar cells into devices that are both easy to fabricate and have high cell power conversion efficiency, on par with those of silicon solar cells [4]. But a marketable perovskite photovoltaic device is still several years down the road, due to its stability issues. [6, 7, 8, 9]

Methylammonium lead iodide ($MAPbI_3$) perovskite, which, as the name suggested, has methylammonium (MA) as the cation, is regarded as the archetype of HOIPs since it exhibits rich fundamental photovoltaic properties, and has recently been intensively studied and developed for solar cell devices. $MAPbI_3$ exists in three phases, namely orthorhombic ($Pnma$) at 0 K $< T <$ 165 K, tetragonal ($I4/mcm$) at 165K $<$ T $<$ 327 K, and cubic ($Pm\bar{3}m$) at T $>$ 327 K with ordered antiferroelectric MA cation arrangement for the first, and disordered arrangements for the latter two. [32, 33, 34, 24] Orientation dynamics of the organic cations is associated with physical properties of $MAPbI_3$. One is the ferroelectric effect which is related to an anomalous hysteresis in the HOIP solar cells. [35] Long migration length of electrons and holes [36], structural evolution and stability are also resulted from the said dynamics. [34, 37, 24, 38, 39, 40, 41, 42, 43].

Recent experimental results suggest that there exist two kinds of dynamics associated with a MA cation in $MAPbI_3$. [42] The first type is the reorientation of the C-N axis with estimated $3 - 14$ ps time scale [36, 35, 42, 38]. The second type is the faster methyl and/or ammonium groups rotation about C-N axis with sub-picosecond time scale. [44] Such fast-rotation cannot be precisely probed by experiments. [42] Moreover, the interplay between octahedron tilting and the MA dynamics still needs a clearer understanding, as it has recently been dubbed as the chicken-and-egg paradox by Li and Rinke. [45]

Since the emergence of HOIPs as photovoltaic materials in 2009 [27], density functional theory (DFT) based calculations have been adopted to study their properties and underlying physics. Many suggest the importance van der Waals (vdW) interaction in the calculations. [46, 45, 47, 48, 43, 49] Nevertheless, there are a number of methods for including the vdW-interaction in the DFT calculations. Each of them yields different levels of accuracy, especially, for molecular and hydrogen-bond materials. The detailed discussions on the methodology and accuracy of the vdW functionals can be found elsewhere. [50, 51, 52]

2.3.2 Band Gap Engineering in $MAPbI_3$

Main property of optoelectronic material that need to be addressed to maximize its potential is the optical band gap, which is governed by the energy band gap in the theoretical perspective. Kong *et al.* has studied the relationship between the structural properties and band gap of various HOIPs. [53] They shown that the change in Pb-I bond length and Pb-I-Pb bond angle both contribute to the change in energy gap of HOIPs. Other experiments also attempted to optimize the material by doping the perovskite layer with inorganic cations such as cesium or rubidium, which shown the improvement in band gap properties. However, doping induces other undesirable changes such as reduced lifetime of the cell or structural distortion. Thus, chemical means of tuning the band gap lead to more problem than it may solve. [5]

CHAPTER III

THEORETICAL BACKGROUND

In this chapter, we describe necessary theories and methods for the understanding of electron behaviors to predict and explain the physical properties in condensed matters.

3.1 Many body problems

In quantum mechanics, Schrödinger's equation share a major success to study and explain the property of a single particle in any given potential. However, their behaviors are hard and complicated to find the exact solution by solving many-body Schrödinger's equation, Eq. (3.1), due to a large number of electron and ion wave functions in the system,

$$\hat{H}\Psi(\mathbf{r}_1, \mathbf{r}_2, ..., \mathbf{r}_{N_e}, \mathbf{R}_1, \mathbf{R}_2, ..., \mathbf{R}_{N_n}) = E\Psi(\mathbf{r}_1, \mathbf{r}_2, ..., \mathbf{r}_{N_e}, \mathbf{R}_1, \mathbf{R}_2, ..., \mathbf{R}_{N_n}), \tag{3.1}$$

where $\hat{H}$ is the Hamiltonian of the many-body system,

$$\begin{aligned} \hat{H} = & -\sum_i \frac{\hbar^2}{2m} \bigtriangledown_i^2 + \frac{1}{2} \sum_{(i \neq j)} \frac{e^2}{|\mathbf{r}_i - \mathbf{r}_j|} - \sum_{i,I} \frac{Z_I e^2}{|\mathbf{r}_i - \mathbf{R}_I|} \\ & - \sum_I \frac{\hbar^2}{2M} \bigtriangledown_I^2 + \frac{1}{2} \sum_{(I \neq J)} \frac{Z_I Z_J e^2}{|\mathbf{R}_I - \mathbf{R}_J|}. \end{aligned} \tag{3.2}$$

The small and capital letters represent electron and ion, respectively. The N_e is an amount of the electrons and N_n is an amount of the ions (or nuclei) in the system. The right hand side terms of Eq. (3.3) consist of the kinetic energy of electrons, electron-electron coulomb interaction, electron-ion coulomb interaction, kinetic energy of ions, and ion-ion coulomb interaction, respectively. For a basic approximation, we can assume that the ions are moving much slowly than the electrons so that the movement of the ions seen motionless, so the last two terms can be set as a constant. The wave functions and Hamiltonian, focused only on the electron parts, is called the Born-Openheimer approximation [54].

The Hamiltonian of the electron system for the ions at rest can be reduced to

$$\hat{H} = -\sum_i \frac{\hbar^2}{2m} \bigtriangledown_i^2 + \frac{1}{2} \sum_{(i \neq j)} \frac{e^2}{|\mathbf{r}_i - \mathbf{r}_j|} + \sum_i v(r_i). \tag{3.3}$$

The $v(\mathbf{r}_i)$, Eq. (3.3), is the electron-ion interaction. In a general case, this term is an external potential which includes external forces in the background. Although, the number of variables in the N_e-body wave functions is reduced to $3N_e$ but it cannot be solved exactly. In 1928, Hatree proposed that the wave functions can be purely separated by multiplication and written as superposition of many one-body wave functions. This is called Hartree approximation [55]. However, the ground state energy calculated is always an overestimation to the exact ground state energy. We know that the electron is a fermion, so it must satisfy Pauli's exclusion principle, which two electrons cannot be filled in the same state. The electron wave function solution, Eq. (3.4) must be antisymmetric and can be satisfied by the Slater determinant. This is called the Hatree-Fock approximation [56].

$$\Psi_{HF} = \frac{1}{\sqrt{N!}} \begin{vmatrix} \psi_1(\mathbf{r}_1) & \psi_2(\mathbf{r}_1) & \cdots & \psi_{N_e}(\mathbf{r}_1) \\ \psi_1(\mathbf{r}_2) & \psi_2(\mathbf{r}_2) & \cdots & \psi_{N_e}(\mathbf{r}_2) \\ \vdots & \vdots & \ddots & \vdots \\ \psi_1(\mathbf{r}_{N_e}) & \psi_2(\mathbf{r}_{N_e}) & \cdots & \psi_{N_e}(\mathbf{r}_{N_e}) \end{vmatrix}$$

$$= \frac{1}{\sqrt{N!}} \det[\psi_1(\mathbf{r}_1)\psi_2(\mathbf{r}_2)\cdots\psi_{N_e}(\mathbf{r}_{N_e})] \tag{3.4}$$

This ground state energy calculated is lower than in the Hartree approximation but it is still higher than the exact ground state energy. The difference energy calculated between the Hartree and the Hartree-Fock energy is called the exchange energy, while the difference energy calculated between the Hartree-Fock energy and the true ground state energy is called the correlation energy. However, there are many methods that can calculate the ground state energy. One of the most popular method is the density functional theory (DFT), which will be explained in section 3.2.

3.2 Density functional theory

Density functional theory (DFT), which was proposed by Hohenberg and Kohn in 1964 [57], is one of the most popular and successful approach to investigate the ground state energy and electronic structure in a many-body system. The DFT describes the probability of an electron being present at a specific location in a periodic system of solid, referred to as the electron density. However, the DFT was not considered accurate enough for theoretical calculations until the 1990s, when some approximations were greatly refined to better model of the exchange and correlation interactions. The Kohn-Sham equation is the most important equation for the DFT calculation, which will be shown in section 3.2.2. And, the exchange-correlation functional details will be explained in section 3.2.3.

3.2.1 Hohenberg-Korn theorem

First, we can write the Hohenberg-Kohn energy functional, $E[n]$, in the form of the electron density functional, $n \equiv n(\mathbf{r})$, as

$$E[n] = T_S[n] + V_H[n] + V_{Ext}[n] + E_{xc}[n] \tag{3.5}$$

where, $T_S[n]$ is the electron kinetic energy of a non-interacting system, $V_H[n]$ is the Coulomb potential energy of electrons or the Hartree potential, $V_{Ext}[n]$ is the external potential energy i.e. the Coulomb potential energy between ions and electrons, and $E_{xc}[n]$ is the interaction between the electrons including the exchange-correlation energy that is different form in each functional. Hohenberg and Kohn used the electron density to explain an inhomogenous electron gas which is reasonable for the electrons in a periodic system [57]. They proposed two important theorems that support the DFT calculation, which are

The first theorem: For the system of interacting particles, there exists only one exact ground state density, $n_0(\mathbf{r})$ that corresponds to an external potential, $V_{Ext}[n]$.

The second theorem: The total energy can be represented in terms of functionals of the electron density. The exact ground state energy, E_0, gives minimum value if and only if the density is the exact ground state density, $n_0(\mathbf{r})$,

$$E_0 = E[n_0(\mathbf{r})] \leq E[n(\mathbf{r})], \tag{3.6}$$

by using the variational principle,

$$\frac{\delta E[n_0(\mathbf{r})]}{\delta n(\mathbf{r})} = 0. \tag{3.7}$$

3.2.2 Kohn-Sham equation

According to Eq. (3.5) and the Hohenberg-Kohn theorems, the non-interacting electron kinetic energy in term of the electron density, $T_S[n]$, was first proposed by Thomas and Fermi based on the uniform electron gas in 1927 [58, 59, 60], as

$$T_{TF}[n] = \frac{3}{10}(3\pi^2)\int n^{5/3} d\mathbf{r}. \tag{3.8}$$

However, this formula is not used in our calculation because its performance is inaccurate. The electron kinetic energy used was proposed by Kohn and Sham in 1965, which was expressed in terms of the Kohn-Sham orbitals, as

$$T_S[n] = \sum_i^N \int \psi_i^{*KS}(\mathbf{r}) \left(-\frac{\hbar^2}{2m}\bigtriangledown^2\right) \psi_i^{KS}(\mathbf{r}) d\mathbf{r} \tag{3.9}$$

where, $\psi_i^{KS}(\mathbf{r})$ is the Kohn-Sham orbital and the electron density can be defined by

$$n(\mathbf{r}) = \sum_{i=1}^N \left|\psi_i^{KS}(\mathbf{r})\right|^2 = \sum_{i=1}^N \psi_i^{*KS}(\mathbf{r})\psi_i^{KS}(\mathbf{r}). \tag{3.10}$$

Next, the second term of Eq. (3.5), $V_H[n]$, is the Coulomb potential energy of electrons or Hartree potential. The constant $\frac{1}{4\pi\epsilon_0}$ is excluded. It can be expressed explicitly as

$$V_H[n] = \int\int \psi_i^{KS}(\mathbf{r})\psi_i^{*KS}(\mathbf{r}) \frac{1}{|\mathbf{r}-\mathbf{r}'|} \psi_j^{KS}(\mathbf{r}')\psi_j^{*KS}(\mathbf{r}') d\mathbf{r} d\mathbf{r}'$$

$$= \int \psi_i^{KS}(\mathbf{r})\psi_i^{*KS}(\mathbf{r}) \int \frac{\psi_j^{KS}(\mathbf{r}')\psi_j^{*KS}(\mathbf{r}')}{|\mathbf{r}-\mathbf{r}'|} d\mathbf{r}' d\mathbf{r}. \tag{3.11}$$

From the electrostatics, the scalar potential, $\Phi(\mathbf{r})$, is generated by

$$\Phi(\mathbf{r}) = \int \frac{\psi_j^{KS}(\mathbf{r}')\psi_j^{*KS}(\mathbf{r}')}{|\mathbf{r}-\mathbf{r}'|} d\mathbf{r}' = \int \frac{n(\mathbf{r}')}{|\mathbf{r}-\mathbf{r}'|} d\mathbf{r}' \tag{3.12}$$

so,

$$V_H[n] = \frac{1}{2}\int \psi_i^{KS}(\mathbf{r})\psi_i^{*KS}(\mathbf{r})\Phi(\mathbf{r})d\mathbf{r}$$
$$= \frac{1}{2}\int n(\mathbf{r})\Phi(\mathbf{r})d\mathbf{r}. \tag{3.13}$$

The coefficient $\frac{1}{2}$ is included to take care of the double counting. Next, the third term of Eq. (3.5), $V_{Ext}[n]$, is the external potential which can be written as

$$V_{Ext}[n] = \int n(\mathbf{r})v_{ion}(\mathbf{r})d\mathbf{r} \tag{3.14}$$

where, $v_{ext}(\mathbf{r})$ is the Coulomb potential from the ion on the single electron at position $(\mathbf{r})$ as

$$v_{ion}(\mathbf{r}) = \sum_I \frac{Z_I e^2}{|\mathbf{r} - \mathbf{R}_I|}. \tag{3.15}$$

The last term of Eq. (3.5), $E_{xc}[n]$, is the exchange-correlation term. The exact total energy is corrected by this term, in which one of the simplest function is

$$E_{xc} = \int \epsilon_{xc} n(\mathbf{r})d\mathbf{r}. \tag{3.16}$$

The total energy in Eq. (3.5) can be written as

$$E[n(\mathbf{r})] = E[\{\psi_i^{KS}(\mathbf{r})\}] = T_s + V_H + V_{Ext} + E_{xc}$$
$$= \sum_i^N \int \psi_i^{*KS}(\mathbf{r}) \left(-\frac{\hbar^2}{2m}\bigtriangledown^2\right) \psi_i^{KS}(\mathbf{r})d\mathbf{r} + \frac{1}{2}\int n(\mathbf{r})\Phi(\mathbf{r})d\mathbf{r}$$
$$+ \int n(\mathbf{r})v_{ion}(\mathbf{r})d\mathbf{r} + \int \epsilon_{xc} n(\mathbf{r})d\mathbf{r}. \tag{3.17}$$

The total energy in Eq. (3.17) is the functional of $n(\mathbf{r})$ or $\psi_i(\mathbf{r})$ which are taken the derivatives of real functions. It is included the normality constraint of each orbital that the number of electrons must be conserved as

$$\sum_i \int \psi_i^{KS}(\mathbf{r})\psi_i^{*KS}(\mathbf{r})d\mathbf{r} = N_e. \tag{3.18}$$

The Euler's equation with a separate Lagrange multiplier (λ_i) can be written as

$$\frac{\delta}{\delta n}\left[E[n]\right] = \frac{\delta}{\delta \psi_i^{*KS}}\left[E\{\psi_i^{KS}\}\right] = 0,$$

$$\frac{\delta}{\delta \psi_i^{*KS}}\left[T_s + V_H + V_{Ext} + E_{xc} - \sum_i \lambda_i \left(\int \psi_i^{KS}\psi_i^{*KS} d\mathbf{r} - N\right)\right] = 0. \tag{3.19}$$

The derivatives on each term of Eq. (3.19) are written as

$$\begin{aligned}
\frac{\delta}{\delta \psi_i^{*KS}} T_s &= -\frac{\hbar^2}{2m} \bigtriangledown_i^2 \psi_i^{KS}, \\
\frac{\delta}{\delta \psi_i^{*KS}} V_H &= \Phi(\mathbf{r})\psi_i^{KS}, \\
\frac{\delta}{\delta \psi_i^{*KS}} V_{Ext} &= v_{ion}(\mathbf{r})\psi_i^{KS}, \\
\frac{\delta}{\delta \psi_i^{*KS}} E_{xc} &= \epsilon_{xc}\psi_i^{KS}, \\
-\sum_i \lambda_i \frac{\delta}{\delta \psi_i^{*KS}} \left(\int \psi_i^{KS}\psi_i^{*KS} d\mathbf{r} - N\right) &= -\lambda_i \psi_i^{KS}.
\end{aligned} \tag{3.20}$$

From Eq. (3.19) and (3.20), the Kohn-Sham equations can be obtained as

$$\begin{aligned}
\left[-\frac{\hbar^2}{2m} \bigtriangledown_i^2 + \Phi(\mathbf{r}) + v_{ion}(\mathbf{r}) + \epsilon_{xc} - \lambda_i\right] \psi_i^{KS} &= 0 \\
\left[-\frac{\hbar^2}{2m} \bigtriangledown_i^2 + V_{eff}[n(\mathbf{r})]\right] \psi_i^{KS} &= E_i \psi_i^{KS}
\end{aligned} \tag{3.21}$$

where, $\lambda_i \equiv E_i$. The effective potential, $V_{eff}[n(\mathbf{r})]$, is defined by

$$\begin{aligned}
V_{eff}[n(\mathbf{r})] &= \Phi(\mathbf{r}) + v_{ion}(\mathbf{r}) + \epsilon_{xc} \\
&= \int \frac{n(\mathbf{r}')e^2}{|\mathbf{r} - \mathbf{r}'|} d^3\mathbf{r} - \sum_I \frac{Z_I e^2}{|\mathbf{r} - \mathbf{R}_I|} + \frac{\delta E_{xc}[n(\mathbf{r})]}{\delta n(\mathbf{r})}.
\end{aligned} \tag{3.22}$$

The Kohn-Sham equation, Eq.(3.21), is the *like* Schrödinger's equation, but it is not Schrödinger's equation because it can be set the electron density on any arbitrary basis set. Moreover, the Kohn-Sham orbitals, ψ_i^{KS}, is not an exact wave function for discussion the properties of one electron in the system. But the ground state density can be obtained from the summation of overall occupied one-electron states.

3.2.3 Exchange and correlation functional

From the Kohn-Sham equation, Eq. (3.21), the exchange-correlation term is only one unknown term which there is no exact form and must be modeled. There are many approximations for the exchange-correlation functionals. Two acceptable approximations that have high accuracy for calculation the physical properties and are the most popular are the local density approximation (LDA) and the generalized gradient approximation (GGA). The LDA assumes that the exchange-correlation energy per electron is known on homogeneous electron gas with the same density at any position $\mathbf{r}$. The approximate functional can be written as

$$E_{xc}^{LDA}[n] = \int n(\mathbf{r})\epsilon_{xc}(n)d\mathbf{r}. \tag{3.23}$$

The $\epsilon_{xc}(n)$ is a function of $n(\mathbf{r})$ at a particular point of space. The LDA is widely used in the slowly varying density systems. However, it is not well described in many cases such as in the rapidly varying density systems. The GGA attempts to improve the LDA by including the gradient of the density, $\bigtriangledown n$, which can be written as

$$E_{xc}^{GGA}[n] = \int n(\mathbf{r})\epsilon_{xc}(n, \mid \bigtriangledown n \mid)d\mathbf{r}. \tag{3.24}$$

3.2.4 Self-consistence field method

The total energy of system can be got by the exact ground state density, $n_0(\mathbf{r})$, which it can be obtained by the Kohn-Sham orbital, ψ_i^{KS}, and the Kohn-Sham equation solving, as follows in Eq. 3.10 and 3.21, respectively. The algorithm for solving the self-consistent Kohn-Sham equation is shown in Figure 3.1.

First, the initial electron density, $n(\mathbf{r})$, is generated to calculate the effective potential, $V_{eff}[n(\mathbf{r})]$, i.e. the $V_H[\mathbf{n}]$ and $V_{xc}[\mathbf{n}]$ terms. Second, the Kohn-Sham equation is solved by the diagonalization matrix to obtain the Kohn-Sham orbital and a new electron density. Next, the total energy is calculated by the new electron density. If the calculated total energy is minimum value, the self-consistent loop will be stopped. If not, a new electron density must be generated by mixing the current and previous densities. Then, the calculation must be repeated again until the total energy is converged.

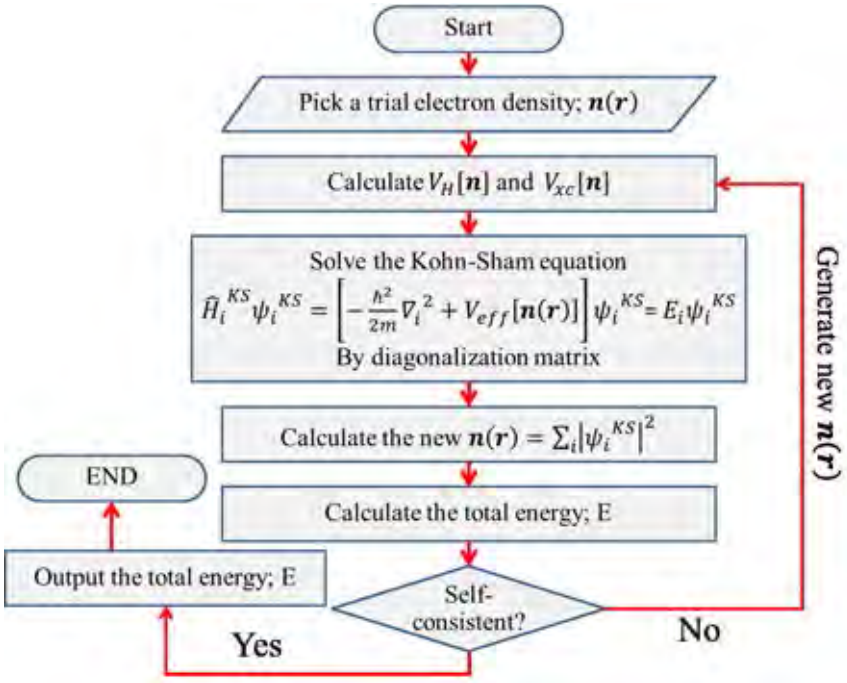

Figure 3.1: Flow chart of the self-consistent field method for the total energy calculation.

3.3 Techniques of calculation on DFT

Although, the DFT calculation is approach to untangle the solution in the many-body problems. However, the Kohn-Sham orbital can be expressed as a linear combination of an arbitrary basis function, $\phi_m(\mathbf{r})$, as

$$\psi_n(\mathbf{r}) = \sum_{m=1}^{L} c_{nm}\phi_m(\mathbf{r}). \tag{3.25}$$

For $L \to \infty$, it would give the exact expression but it uses large calculation resources. However, a few number of basis functions are required in reasonably accurate calculations. Both the CASTEP and the Quantum-ESPRESSO codes are used in this thesis. They are chosen the plane wave (PW) basis set which is a complete and orthogonal set that satisfies the Bloch's theorem. The PW basis set will be discussed in Section 3.3.1. The accuracy and precision of the Kohn-Sham equation calculations depend on the number of PW basis sets. But they used more computational resources, i.e. time and space, for calculation. Thus, The pseudopotential method, the cutoff energy, and the k-point mesh are important factors to determine the number of the PW basis sets, are discussed in Section 3.3.2 and 3.3.3, respectively.

3.3.1 Plane wave basis set

The electron wave functions were proved by F. Bloch, that are the solutions of the Schrödinger's equation for the periodic potential system, must be of a special form as [61, 62],

$$\Psi(\mathbf{r}) = e^{i\mathbf{k}\cdot\mathbf{r}}U(\mathbf{r}), \tag{3.26}$$

where $\mathbf{k}$ is wave vector. The $U(\mathbf{r})$ is the periodic arbitrary function of the crystal lattice and satisfies the periodicity in the solid. It has to follow the Bloch's theorem,

$$U(\mathbf{r}) = U(\mathbf{r} + \mathbf{T}), \tag{3.27}$$

where $\mathbf{T}$ is the translation vector of the lattice. In order to follow the Bloch's theorem, the electron wave function is written as

$$\Psi(\mathbf{r} + \mathbf{R}) = e^{i(\mathbf{k})\cdot\mathbf{R}}\Psi(\mathbf{r}). \tag{3.28}$$

Then, the periodic function, $U(\mathbf{r})$, can always be expressed as the Fourier's series to be

$$U(\mathbf{r}) = \sum_{\mathbf{G}} u_{\mathbf{G}} e^{i\mathbf{G}\cdot\mathbf{r}}, \tag{3.29}$$

where $\mathbf{G}$ is the reciprocal lattice vector. By the Fourier's transformation, the electron wave functions can be written as,

$$\Psi(\mathbf{r}) = \frac{1}{\Omega}\sum_{\mathbf{n}} \Psi(\mathbf{k} + \mathbf{G}_n)e^{i(\mathbf{k}+\mathbf{G}_n)\cdot\mathbf{r}} \tag{3.30}$$

where Ω is the volume of the system.

3.3.2 Pseudopotential method

The DFT calculation using all electron wave functions give the excellent accuracy results. However, the PW basis sets are good for explaining the valence and nearly free-electrons. In order to explain the core electrons, a large number of the PW basis sets are required because they have strong interacting with the nucleus of atoms. The all electron wave functions can be separated into two parts, which are the core and valence wave functions. In 1959, Phillips and Kleinman [63, 64] proposed that the valence wave

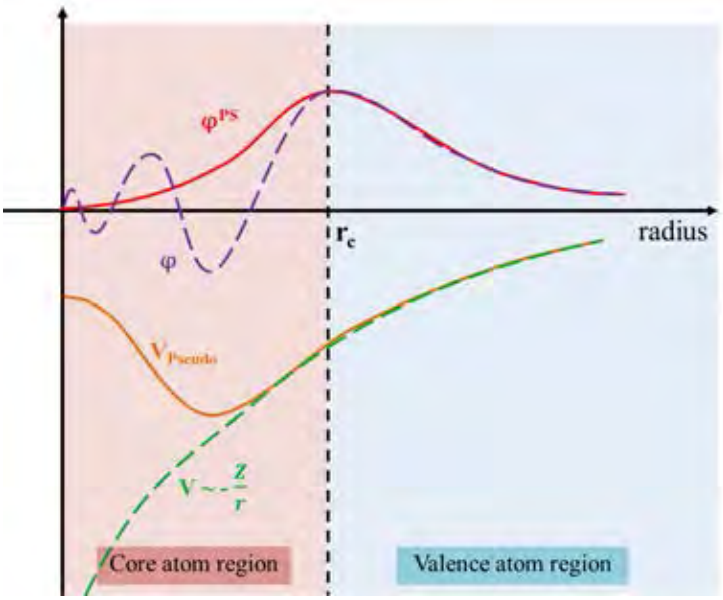

Figure 3.2: Pseudo wave function and pseudopotential.

function, φ^v, in core atom region is divided by core radius, r_c into two parts,

$$\varphi^v = \varphi^{ps} - \sum_n a_n \varphi_n^c, \tag{3.31}$$

where φ_n^c is the core wave function, φ^{ps} is the pseudo wave function (red line shown in Figure 3.2) which is a smooth part of the valence wave functions, and the summation term is the oscillating part in the core atom region of the valence wave functions.

In 1979, Hamann et al. [65] proposed the conditions to provide the accuracy of the pseudo wave function, is called the norm-conseving pseudopotential. The conditions are

1. The real and pseudo eigenvalues are equal,

$$\epsilon^v = \epsilon^{ps} \tag{3.32}$$

2. The real and pseudo wave functions outside the core region, $r > r_c$, are the equivalent,

$$\varphi^v(\mathbf{r}) = \varphi^{ps}(\mathbf{r}); r \geq r_c \tag{3.33}$$

3. The integrals from 0 to r_c of the real and pseudo charge densities are the equivalent,

$$\int_{r<r_c} |\varphi^v(\mathbf{r})|^2 r^2 d\mathbf{r} = \int_{r<r_c} |\varphi^{ps}(\mathbf{r})|^2 r^2 d\mathbf{r} \tag{3.34}$$

4. The first energy derivatives of the logarithmic derivatives of the real and pseudo wave function are equivalent for$r > r_c$.

The conditions of the norm-conserving pseudopotentials are too limited and unsuitable for some systems. In 1990, Vanderbilt [66] showed that the norm-conserving constraint can be discount the numbers of plane waves in the calculation and also increase the speed of calculation, is called the ultrasoft pseudopotential.

3.3.3 Cutoff energy and k-point

The reciprocal space (**k**-space) represents the Fourier transform of the periodic lattice in real space. The simplest definition of the first Brillouin zone is the Wigner-Seitz primitive unit cell of the reciprocal lattice, where **G** is the reciprocal lattice vector. In our calculation, the Kohn-Sham equation, in Eq. 3.21, is solved in reciprocal space using the PW for basis sets. The infinite number of the PW basis sets, in form of Eq. 3.30, gives the exact Kohn-Sham solution. However, it cannot be calculated because of the limitation of calculation. So, the suitable number of the PW basis sets is described by the cutoff energy, E_{cut}, which related with the maximum of reciprocal lattice vector, G_{max}. The cutoff energy is defined by

$$E_{cut} \leq \frac{\hbar^2}{2m} |\mathbf{k} + \mathbf{G}_{max}|^2. \tag{3.35}$$

The k-point mesh in the first Brillouin zone can be chosen which proposed by Monkhorst and Pack, in 1976 [67]. The larger number of the cutoff energies and the k-points gives more accurate calculation but it also requires more computational resources. Thus, the convergence test of cutoff energy and k-point must be examined which these details will be discussed in Chapter 4.

3.4 Geometry optimization

The geometry optimization is the approach to find the ground state structure which the crystal structure can be relaxed. We well-known that the temperature is ignored, T

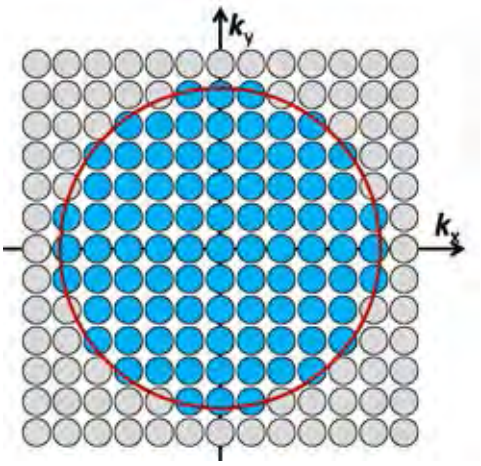

Figure 3.3: Cutoff energy (shown in red circle), and k-point grid in reciprocal space.

= 0 K in the DFT calculation. Then, the enthalpy, $\mathcal{H}$, must be minimized with regard to satisfy the applied external pressure, P. The enthalpy is defined by

$$\mathcal{H} = E + PV, \tag{3.36}$$

where E is the total energy and V is the volume of the system. The enthalpy is the functional of the strain tensors, ϵ, and the coordinates of the atomic positions, $\mathbf{r}$, [68] as

$$\mathcal{H} \equiv \mathcal{H}(\epsilon, \mathbf{r}_1, \mathbf{r}_2, ..., \mathbf{r}_N). \tag{3.37}$$

For N atoms in unit cell, the enthalpy has $(9 + 3N)$-dimensions where 9-dimensions are of the strain components (3 extensional and 6 shear strains) and $3N$-dimensions are of the coordinates of the atomic positions. The force vector, F, at the pressure, P, can be calculated by the negative of the first derivative of the enthalpy respect to the column vector, X, as

$$F = -\frac{\partial \mathcal{H}}{\partial X}\bigg|_P. \tag{3.38}$$

The components of column vector are defined as

$$X_{3(i-1)+j} = \epsilon_{ij}; i, j = 1, 2, 3, \tag{3.39}$$

and the followers are the coordinates of the atomic positions in the unit cell. The variation of the enthalpy around the minimum X_{min} is

$$\delta\mathcal{H} = \frac{1}{2}(X - X_{min}) \cdot B(X - X_{min}), \tag{3.40}$$

where B is the Hessian matrix.

We used the quasi-Newton method which is a root finding algorithm to search the minimum of the column vector, X_{min}, from the force, F, in a relaxation step of unit cell. The column vector, X, in step $(n+1)^{th}$ is generated by

$$\begin{aligned} X_{n+1} &= X_n + \alpha_n \Delta X_n, \\ X_n &= H_n F_n, \end{aligned} \tag{3.41}$$

where α_n is a step length and H_n is the inverse of the Hessian matrix, $H = B^{-1}$. Normally, the initial Hessian matrix, H_0, is set to be the identity matrix, $\mathbf{I}$. Then, it is evolved by the Broyden–Fletcher–Goldfarb–Shanno (BFGS) algorithm [68]. Thus, if the X gets to the minimum, the crystal structure will satisfy the external pressure and it also gives the calculated minimum enthalpy. It means the final calculated crystal structure is the most stable under the external pressure conditions.

3.5 Electronic band structure

The solution of the Kohn-Sham equation, Eq. 3.21, gives the ground state wave function, $\psi_{n,k}$, and also corresponding the Hamiltonian, $\hat{H}$, of the solid system. The electronic properties of the system can be obtained by the first Brillouin zone in the reciprocal space. The energy eigenvalue, ϵ, k, of the n^{th} energy level at wave vector, $\mathbf{k}$, are obtained by

$$\langle \psi_{n,k} | \hat{H} | \psi_{n,k} \rangle = \epsilon, k. \tag{3.42}$$

From Eq. 3.5, the electronic band structure is investigated by plotting these energy eigenvalues in the k-point paths through the high symmetry directions in the first Brillouin zone.

3.6 Density of states

The density of states (DOS) define that the number of the electrons which are available at an energy level (energy state) . The DOS for a given n^{th} energy level, $N_n(E)$, can be written as

$$N_n(\epsilon) = \frac{1}{4\pi^3} \int \delta(\epsilon - \epsilon_n(\mathbf{k}))d\mathbf{k}, \tag{3.43}$$

where $\epsilon_n(\mathbf{k})$ is the energy eigenvalue of the n^{th} energy level in the k-points. The partial density of states (PDOS) is the projection of the DOS in the attentive eigenstates. Maybe, it is called the projected density of states. The total DOS is obtained from the summation of all bands in valence band region, which are represented by total of electrons in unit cell.

CHAPTER IV

STRUCTURE OPTIMIZATION OF CUBIC $MAPbI_3$ AT AMBIENT PRESSURE

Density-functional-theory-based calculations are sensitive to parameter set-ups. In this chapter, we set out to evaluate the convergence criteria for each parameters for the system in consideration. Then, with the converged results, we compare our calculation with experimental data. The calculation set-up configurations chosen in this chapter are adopted by all works following this thesis book's chapter.

4.1 Introduction

As discussed in Chapter III, density functional calculations will be insightful only when the calculation parameters are properly chosen. Higher wavefunction cutoff energies and denser k-point meshes give more accurate results, but how accurate is 'adequate'? The convergence tests are designed to evaluate the accuracy of the DFT calculations. It is the test that must be rigorously taken before any real DFT calculation can take place. A well-converged calculation resembles the physical system. Whereas the unconverged calculation are meaningless.

In addition to the convergence test, the simulated results are compared with the data from experiment to justify the accuracy of the DFT results.

4.2 The Convergence Test

In previous chapter, we've discussed the meaning of two central terms that define the accuracy of the DFT calculations: the wavefuction cutoff energies and the Monkhorst-Pack k-point grid density, or the E_{cut} and k-point mesh, respectively.

A properly converged calculation is the calculations done with E_{cut} and k-point mesh which give the output total energy difference within a user-defined tolerance. For most cases, the acceptable energy tolerance is set to be within 4 meV per atom, which is

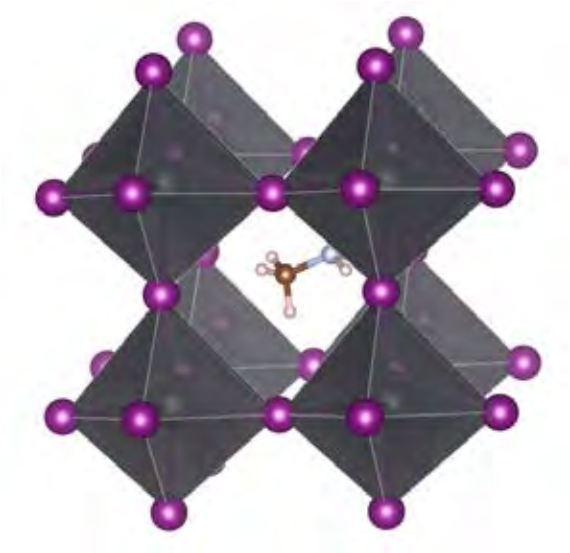

Figure 4.1: A pseudocubic unit cell of $MAPbI_3$.

the estimate value of k_BT where T=273 K.

Note that, it is a good practice to carry out convergence test for every atomic configurations.

Another point to take into consideration when doing a convergence test is the computational resource it takes to do one self consistence calculation. Sometimes increasing k-point mesh to a very fine grid but keep E_{cut} relatively low may make the calculation converged the same way as increasing the E_{cut} values very high but fix the k-point mesh at a lower value. If both configurations give converged result, then the one that consumes less computational resource is usually adopted.

4.2.1 Procedure

The procedure of a convergence test is straightforward. First, we decide for a convergence goal, in our calculation, it is set to 2 meV per cell. Then, for an atomic configuration, a series of self consistence energy calculations are performed. For each self consistence energy calculation, we require a pair of E_{cut} and k-point mesh values determined. Then the simulation will give the total energy. Next, we increase one parameter and reiterate, thus obtaining another ground state energy. The energies of the two steps are compared (i.e. we subtract the energies of the two iterations to obtain the energy difference). The steps are repeated until the difference is smaller than the defined

convergence goal. That is when we accept that the set-up give converged result.

In our convergence test, we used the input atomic position of cubic $MAPbI_3$ from those reported by Brivio *et al* study [34] (available online [69]). The functional used in the test is PBEsol. We vary the E_{cut} from 40 Ry to 120 Ry, with 5 Ry increment between each step. For the k-point mesh, an equal mesh of $n \times n \times n$, were used, where n ranges from 2 to 10, with an increment step of 2. Equally-spaced k-point meshes were selected because the structure is cubic, which transforms into cubic Brillouin zone in k-space. Full input configuration, the lattice parameters and atomic position are given in Table A.1 in Appendix A.

4.2.2 Results and Analysis

Figure 4.2 shows total energy (in eV). Each line represents one k-point mesh set-up and the horizontal axis is the E_{cut} in Rydberg. The result from $2 \times 2 \times 2$ and $4 \times 4 \times 4$ k-point mesh give large error comparing to other values so they are opted out. Detailed view of fig.4.2 is given in fig.4.3. All k-point set-up shown in this figure gives converging E_{cut} in similar trend. We have tested and found that $6 \times 6 \times 6$ k-point gives converged result. Finally, fig.4.4 shows E_{cut} difference graphically. From the figure, E_{cut} equals to 70 Ry gives converged result at 2 meV, which translates into 0.17 meV/atom, so it is chosen to be the standard of further calculations.

Thus, for subsequent calculations on the cubic $MAPbI_3$ perovskite, the kinetic energy cut-off is set to 70 Ry. The unshifted k-point mesh is gridded into $6 \times 6 \times 6$ by Monkhorst-Packs scheme.

4.3 Accuracy of Calculated Structural Parameters Comparing to Experimental Data

Another way to evaluate the accuracy of simulation results is to compare them with reported experimental data. In this section, we performed variable-cell optimization using different functionals that include van der Waals interactions. The relaxation algorithm of atoms and lattice parameters used is Broyden-Fletcher-Goldfarb-Shannon (BFGS) algorithm with a force/atom tolerance equal to 0.001 Hatree/Bohr. The nonlocal vdW exchange correlation(xc) functionals considered in this work are as follows: rvv10 [70],

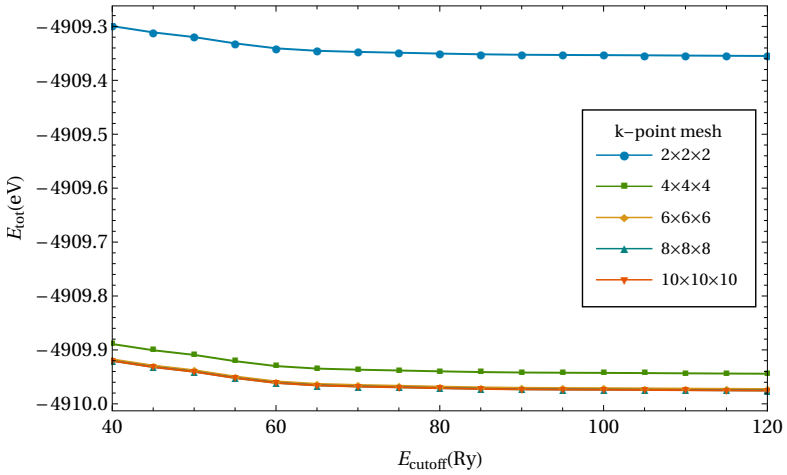

Figure 4.2: Total energy plot for the convergence test.

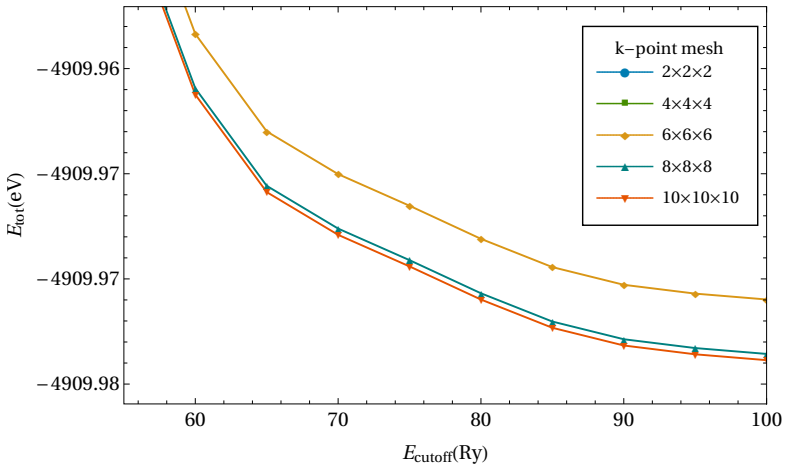

Figure 4.3: Total energy plot for the convergence test, E_{cut} between 50 Ry and 100 Ry.

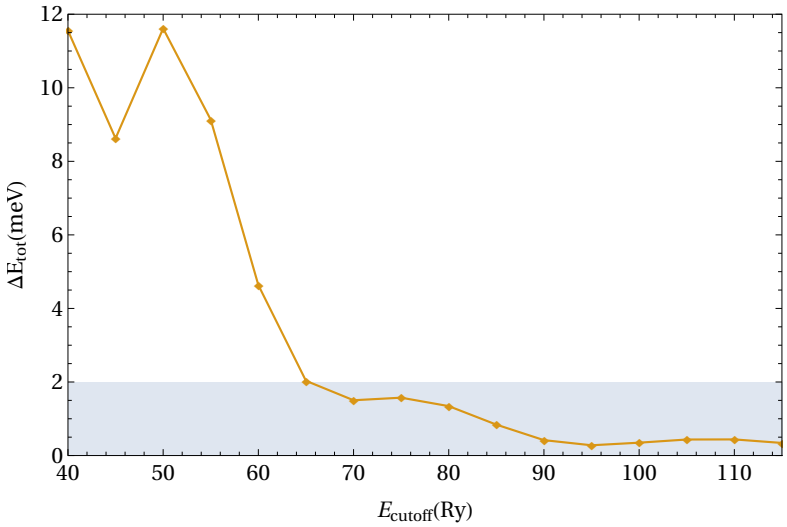

Figure 4.4: Total energy difference for k-point mesh $6 \times 6 \times 6$.

Structural parameters (Å)	$\bar{a}$	$\overline{\textbf{Pb-I}}$	**MAE**(1)	**C-N**	$\overline{\textbf{C-H}}$	$\overline{\textbf{N-H}}$	**MAE**(2)
PBE	6.47050	3.2054	0.1000	1.492	1.094	1.040	0.097
PBEsol	6.29909	3.1456	0.0156	1.484	1.100	1.047	0.098
rVV10	6.37334	3.1833	0.0404	1.503	1.093	1.040	0.100
vdW-DF	6.55397	3.2371	0.1576	1.513	1.090	1.036	0.101
vdW-DF2	6.56195	3.2582	0.1721	1.524	1.087	1.036	0.104
vdW-DF2-b86r	6.35676	3.1728	0.0268	1.496	1.097	1.043	0.100
vdW-DF-cx	6.32021	3.1494	0.0061	1.493	1.098	1.044	0.100
vdW-DF-ob86	6.32862	3.1534	0.0083	1.497	1.097	1.043	0.100
Exp.	6.31728	3.1586	-	1.348	0.994	0.994	-

Table 4.1: Calculated structural parameters (in average) using semi-local and nonlocal vdW functionals compared with experimental results.

vdW-DF [71, 72], vdW-DF2 [73], vdW-DF-ob86 [74] and vdW-DF-cx [75]. The Perdew-Berk-Herzanhoft (PBE) [76] and PBEsol [77] functionals are also used for comparison. The detailed on exchange terms included in each nomenclature are given in **??**.This is our first attempt to evaluate the differences of each van der Waals interactions. We have included almost all van der Waals interactions available in Quantum Espresso 6.0 in this study for the sake of completion. The choice whether to include each algorithm or not is based on its robustness, thus we have omitted outdated ones.

Experimental data were taken from powder neutron diffraction results reported in Weller *et. al.*'s work [24] which assigned $Pm\bar{3}m$ symmetry to $MAPbI_3$ at high temperature. In concordance with the experimental results, the average of calculated parameters from each calculation are used, including average lattice constant ($\bar{a}$), average Pb-I bond length over three inequivalent I-atoms ($\overline{\text{Pb-I}}$), average C-H bond length ($\overline{\text{C-H}}$), average N-H bond length ($\overline{\text{N-H}}$), and C-N bond length (C-N). The resulted structural parameter are are shown in Table 4.1.

The structural parameters are grouped into two subgroups according to their length scale, *i.e.* $\bar{a}$ and $\overline{\text{Pb-I}}$ as one group and C-N, $\overline{\text{C-H}}$ and $\overline{\text{N-H}}$ as another. The mean absolute error (MAE) is used to measure how close the calculations are to the experiment.

The mean absolute error is given by

$$\text{MAE} = \frac{1}{n}\sum_{i=1}^{n}|y_i - \hat{y}_i| = \frac{1}{n}\sum_{i=1}^{n}|e_i|\,. \tag{4.1}$$

Where

$$\text{AE} = |e_i| = |y_i - \hat{y}_i|$$

$$\text{Experiment} = y_i$$

$$\text{Calculation} = \hat{y}_i$$

The parameter $\bar{a}$ and $\overline{\text{Pb-I}}$ are in good agreement with experiment (with MAE$<1\%$) for most xc-functionals, except for vdW-DF, vdW-DF2, and PBE functionals. From all selected functionals, vdW-DF-cx shows the best performance in predicting the lattice constant and the Pb-I distance. This is in agreement with the van der Waals functional testing performed by Berland and Hyldgaard which compares the accuracy of vdW-df-cx with the other functional in predicting the binding energy and equilibrium separation in H-bond and dispersive-force dominated systems [50]. MAE(2) in Table 4.1 shows that C-N, $\overline{\text{C-H}}$, and $\overline{\text{N-H}}$ results are in approximately the same order of error for all functionals, with error of $\sim 10\%$ for C-N and $\overline{\text{C-H}}$, and $\sim 5\%$ for $\overline{\text{N-H}}$.

The disordered C-N axis orientation and the fast on-axis rotation of H-atoms could probably be responsible for the errors in structural parameters. The divergence from the experimental data might originate from the indistinguishability of the atomic position reported by the experiment. Since the position of C and N atoms, and $\text{H}_\text{C}/\text{H}_\text{N}$ cannot be captured experimentally due to the MA dynamics. Their assigned positions are that of the approximation assigned to Wyckoff sites 4MM(100) and 1 of the $\text{Pm}\bar{3}\text{m}$ space group [24]. From the simulation viewpoint, by using only one psuedocubic primitive unit cell, the disordered nature of the organic cations is neglected, giving rise to the divergence from averaged value of the experiment data. Moreover, the effects of temperature which drive atoms from their zero-Kelvin equilibrium configurations was also not included. Although the simulations give large MAE(2), the lattice constant and the Pb-I bond length are in good agreement of with those of the experimental results. The latter validates the use of computational model for investigating the local structural and energetic responses to the rotation of H atoms about their C-N axis.

4.4 Conclusion

The static DFT calculation is performed with the psuedopotential and plane wave method implemented in Quantum-Espresso package[78]. The core ions are represented by original scalar relativistic ultrasoft pseudopotentials taken from PSlibrary project [79]. Spin-orbit coupling (SOC) effects are not included in this work, as previous study suggested that SOC does not significantly affect ground state properties of this material. [80] The kinetic energy cut-off is set to 70 Ry. The unshifted k-point mesh is gridded into $6 \times 6 \times 6$ by Monkhorst-Packs scheme [81]. This configuration yields convergence of total energy within 2 meV, which translates into 0.17 meV/atom. The nonlocal vdW exchange correlation(xc) functionals considered in this work are as follows: rvv10, vdW-DF, vdW-DF2, vdW-DF-ob86 and vdW-DF-cx. The Perdew-Berk-Herzanhoft (PBE) and PBEsol functionals are also used for comparison. The relaxation algorithm of atoms and lattice parameters used is Broyden-Fletcher-Goldfarb-Shannon (BFGS) algorithm with a force/ atom tolerance equal to 0.001 Hatree/Bohr.

The disordered C-N axis orientation and the fast on-axis rotation of H-atoms could probably be responsible for the errors in structural parameters. Although the simulations give large error in the C-N and C/N-H bond lengths, the lattice constant and the Pb-I bond length are in good agreement of with those of the experimental results. The latter validates the use of computational model for investigating the local structural and energetic responses to the rotation of H atoms about their C-N axis.

CHAPTER V

METHYLAMMONIUM DYNAMICS AT AMBIENT PRESSURE

In this chapter, we investigate the effects of MA rotation on structural properties of cubic $MAPbI_3$ at ambient pressure. To simulate the rotational dynamics of MA cation using the DFT calculation, which is, on the contrary, a static simulation, a novel strategy is introduced. We chose $MAPbI_3$ in cubic phase as the subject of our study, since it has only one formula unit per cell, to exclude the effect of multiple MA molecules orientation in a single simulation. Initial structure is that reported by Brivio *et al* study [34] (available online [69]), re-optimized with our settings. Optimization parameters obtained in the preceding chapter were applied in this chapter, where we have compared and discussed accuracy of different van der Waals interactions.

First, some assumptions on the dynamics are outlined in order to apply the DFT-based calculations on this system. The physical interpretation of each model are then discussed. Finally after the analysis section, we have concluded the possible dynamics occurring in $MAPbI_3$ perovskite.

5.1 Introduction

Recent experimental results suggest that there exist two kinds of dynamics associated with a MA cation in $MAPbI_3$.[42] The first type is the reorientation of the C-N axis with estimated $\sim 3-14$ ps time scale [42, 36, 35, 38]. The second type is the faster methyl and/or ammonium groups rotation about C-N axis with sub-picosecond time scale[44]. Such fast-rotation cannot be precisely probed by experiments[42]. Moreover, the interplay between octahedron tilting and the MA dynamics still needs a clearer understanding, as it has recently been dubbed as the chicken-and-egg paradox by Li and Rinke[45].

Since the emergence of HOIPs as photovoltaic materials in 2009 [27], density functional theory (DFT) based calculations have been adopted to study their properties and underlying physics. Many suggest the importance van der Waals (vdW) interaction in

Figure 5.1: Methylammonium molecule viewed from side and head on, showing 3-fold symmetry.

the calculations.[46, 45, 47, 48, 43, 49] Nevertheless, there are a number of methods for including the vdW-interaction in the DFT calculations. Each of them yields different levels of accuracy, especially, for molecular and hydrogen-bond materials.

In this chapter, the author mainly studied the reorientation of MA cation in cubic $MAPbI_3$ perovskite and discussed the hydrogen bonding between the organic molecule and the inorganic octahedron cage at a given C-N axis direction. We focus on equilibrium structural configurations when methyl and ammonium groups are coherently rotated around C-N axis of MA cation. The effect of applications of various vdW density functionals was also investigated. The results obtained demonstrates differences in the rotational potential energy surface (PES) and the optimized configurations for different vdW functionals. These mark out the importance including the vdW interaction in the DFT based studies of dynamics in the $MAPbI_3$.

5.2 Assumptions on Methylammonium Dynamics

5.2.1 Physical Interpretation

We have lengthly reviewed the reorientation of MA ion studied experimentally and theoretically in chapter 2. To summarize, it is possible for the MA ion to rotate about its C_{3v} symmetry axis but the effect of the rotation on the structural properties is still controversial. By rotation, we now consider only the rotation of MA about its C_{3v} symmetry axis, unless specifically restates otherwise. It is likely that the molecule will act as a rigid rotor, with the shape shown in fig.5.1. We may view $MAPbI_3$ system to be composed of two parts, i) the MA molecule and ii) the inorganic octahedra network, that interact with

each other. The MA molecule and the inorganic atoms may interact in different ways. These explanation along with the projected outcome of each scenario are the assumption on MA dynamics we had in mind when performing the DFT calculation.

SCHEME A If we assume that the octahedral network responses quickly to the rotation, then the whole system would assume the lowest energy state along with the rotation. The whole system is 'relaxed' and always assumes the lowest energy possible. This is similar to assuming that the inorganic framework distortion is due to the MA reorientation. The MA rotation 'pulls' the lead and iodine atoms along.

SCHEME B We may also assume that the inorganic atoms would adjust 'partially' to the MA rotation. By partially, the reorientation of both the MA molecule and the inorganic atoms are allowed but the lattice as a whole still retains its original shape.

SCHEME C However, if we assume that the MA molecule rotates in such a manner that it cannot pull the inorganic atoms with it, the inorganic atoms would remain in place while the MA molecule spins in the void. Hence in this scenario, we assume that the inorganic network are not distorted by the rotation, *i.e.* the response of inorganic atoms are not fast enough to catch up with the rotating MA molecule. The inorganic framework would 'not relax' in this model.

5.2.2 Modeling Schemes

Since MA molecule has C_{3v} symmetry, 120° rotation transform on the molecule is equivalent to full 360° rotation. Hence, we may repeatedly rotate the MA molecule of the initial atomic position by 10° for 12 times to mimic the full rotation. The inorganic atoms are kept in their original position. We now have 13 input atomic configurations, which are then used as input position for each model of structural optimization. Graphical methodology is illustrated in Fig.5.2.

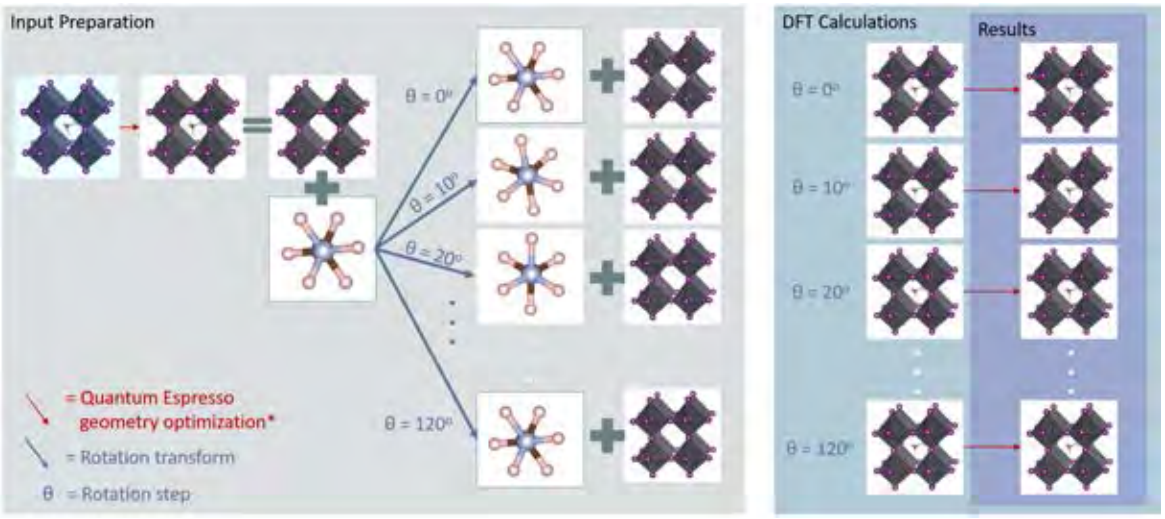

Figure 5.2: Graphical methodology of MA dynamics modeling.

For each mentioned scenario in previous section, we carefully modeled each structural optimization scheme to represent their behavior. Each models are named for further readability. The models are sort in order of ascending optimization restriction.

relax Represent **scheme A**. The initial structure is taken from variable-cell structural optimization from Chapter 4. No restrictions were placed on the cell nor atoms

fix:cell Represent **scheme B**. The initial structure is perfect cubic structure. When performing optimization, the lattice parameters are kept fixed but all atoms are relaxed freely.

fix:cell+PbI_3 Represent **scheme C**. The initial structure is perfect cubic. (Same as *fix:cell*). When performing optimization, the lattice parameters, and Pb and I atoms position are kept fixed. Only MA molecule is relaxed.

Input lattice parameters and atomic position for all schemes are listed in Appendix A.

5.3 Analysis

5.3.1 Energy Barrier

Firstly, we have performed *relax* optimization to further test the difference of van der Waals functionals. Energy barrier of rotation is calculated from

$$\Delta E^i_{tot} = E^i_{tot} - E^0_{tot} \tag{5.1}$$

Where E^i_{tot} is total energy of i^{th} rotation step and E^0_{tot} is the total energy of initial step, which has been listed in Table4.1. Energy barrier is interpreted as the energy needed for the system to transform into another phase, in this case, it shows the energy needed for MA molecule to rotate.

Fig 5.3 shows energy barrier obtained using different van der Waals functional and using PBEsol functional in *relax* optimization. All profiles are mostly symmetric about rotation degree equals to 60° axis. From the result, PBEsol functional gives distinct energy profile from those of van der Waals functionals. When the van der Waals interaction is not included, the barrier shows 3 extrema at 20°, 60° and 100°. However, when the van der Waals interactions are included, the energy barriers have generally broader peak profiles. At 60°, the maximum that is prominent in PBEsol smears out in vdW-DF and vdW-DF2 and morphs into minimum in other cases. Except for vdW-ob86 and rvv10, the concaved peak at 60° originates from ∼0.001 eV difference in total energy of neighboring data point, which is smaller than energy convergence threshold of this study. In addition, the system with van der Waals interaction yields overall lower energy barrier.

The result suggests that van der Waals interaction modifies the ground-state total energy of system with different MA orientation. Since differing van der Waals interactions yield similar energy barrier profile, we have chosen one functional to represent the group hereafter. We opted for vdW-DF-cx for three reasons: 1) its lattice parameter prediction accuracy, 2) its energy barrier profile falls in the norm of other functionals, and 3) the functional was reported to outperform other functionals. This van der Waals functioal testing was done by Berland and Hyldgaard, which compares the accuracy of vdW-DF-cx with other functionals in predicting the binding energy and equilibrium separation in H-

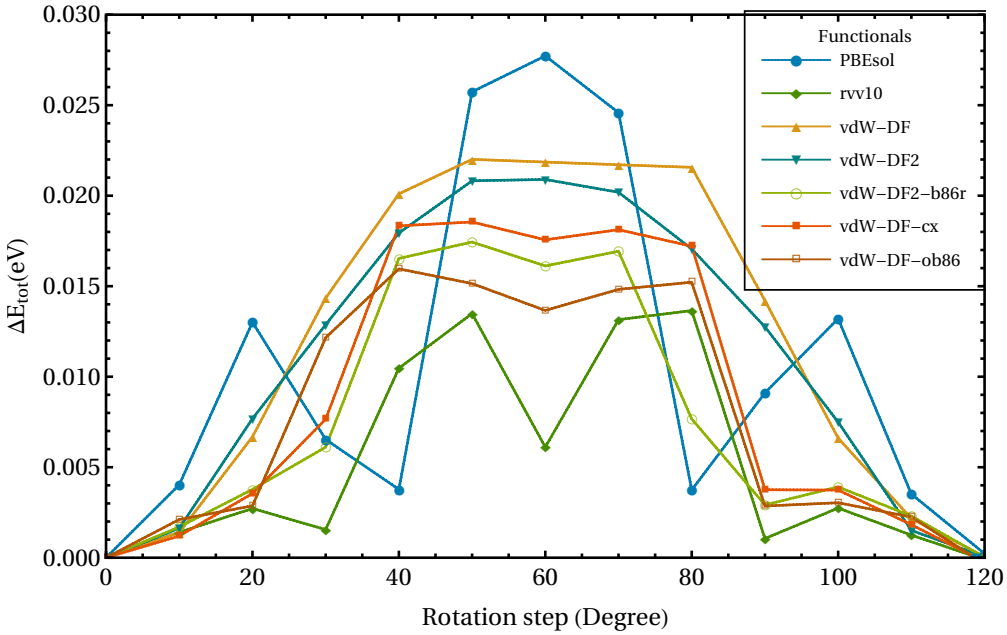

Figure 5.3: Energy barrier plot of *relax*

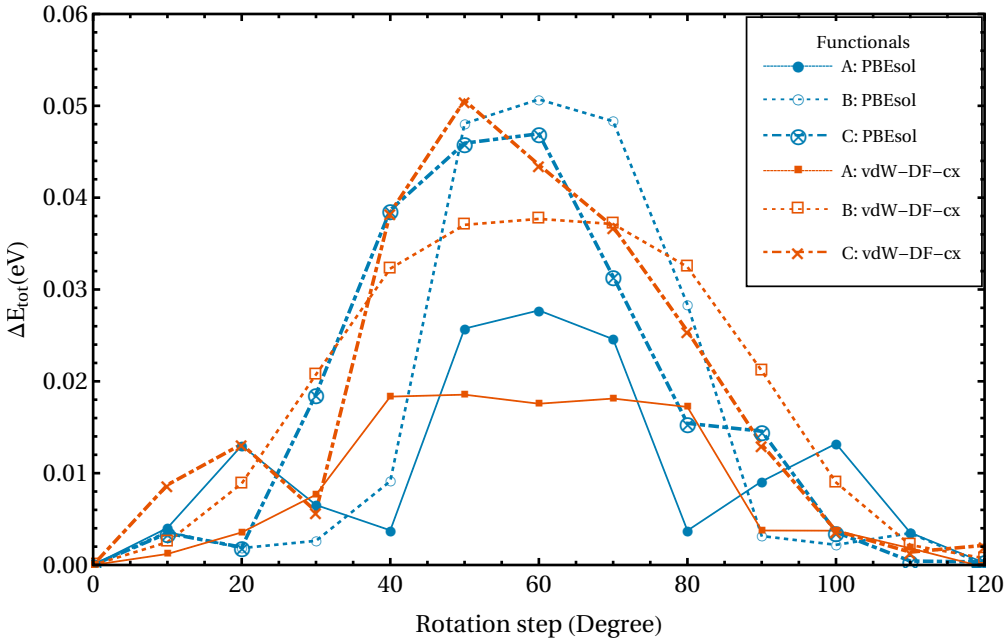

Figure 5.4: Energy barrier plot of *relax* , *fix:cell* and *fix:cell+PbI_3* optimization with PBEsol and vdW-DF-cx functionals, denoted by A, B and C, respectively, in the figure.

bond and dispersive-force dominated systems. [50] May results from other van der Waals functionals be available, they are included in Appendix C, but will not be specifically discussed.

Next, we plot energy barrier obtained from the other two optimization schemes,*fix:cell* and *fix:cell+PbI_3* , optimized with PBEsol and vdW-DF-cx to contrast the contribution of non-local contribution. The result is shown in fig.5.4, note that the vertical axis is doubled of fig.5.3. The most prominent result is that the energy barrier of *fix:cell* and *fix:cell+PbI_3* are 50% greater than that of *relax* . This implies that, if our assumption is valid, the system is less likely to retain its lattice parameter in MA rotation dynamics, and the inorganic network need to adjust to minimize its ground-state energy.

The barrier profile of *fix:cell+PbI_3* for both PBEsol and van der Waals functionals are also significantly unsymmetrical, in contrast with the other two schemes.

Next, we compare results obtained using van der Waals interaction. Among all three optimization schemes, *relax* yields lowest total energy for all rotation steps, except at 30° where both *relax* and *fix:cell+PbI_3* have approximately equal energy barrier. However, this is not the case when optimized with PBEsol. While *relax* yields lowest total energy in the 'middle' rotation angles, *i.e.* between 40° and 80°, the smaller maxima profile of *relax* PBEsol at 20° and 100° make this optimization scheme have the highest energy barrier at these specific angles.

5.3.2 Lattice Parameters

Next, we analyze the relationship between rotational step, lattice parameters and exchange functionals of *relax* optimizations. Fig.5.5 and fig.5.6 shows lattice constant (in Angstrom) and axial angle (in degree) obtained from PBEsol and vdW-DF-cx. Bold lines in all figures denote average value and dashed lines are each specific values, as described in the caption (and by line dashing). We differentiate the functionals by color.

First, from 5.5, the average lattice constant from PBEsol varies with wider range (6.27–6.30 Angstrom) than that of vdW-DF-cx (6.31-6.32 Angstrom). This corresponds to energy barrier result from previous subsection. The profile of the lattice parameter also inversely proportional to the energy barrier profile. Around rotation angle 60° where

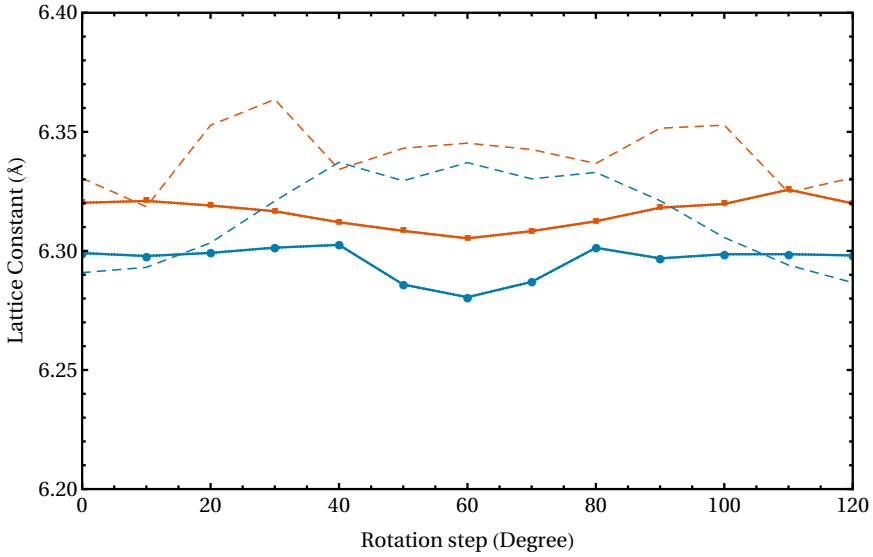

(a) Lattice constant a

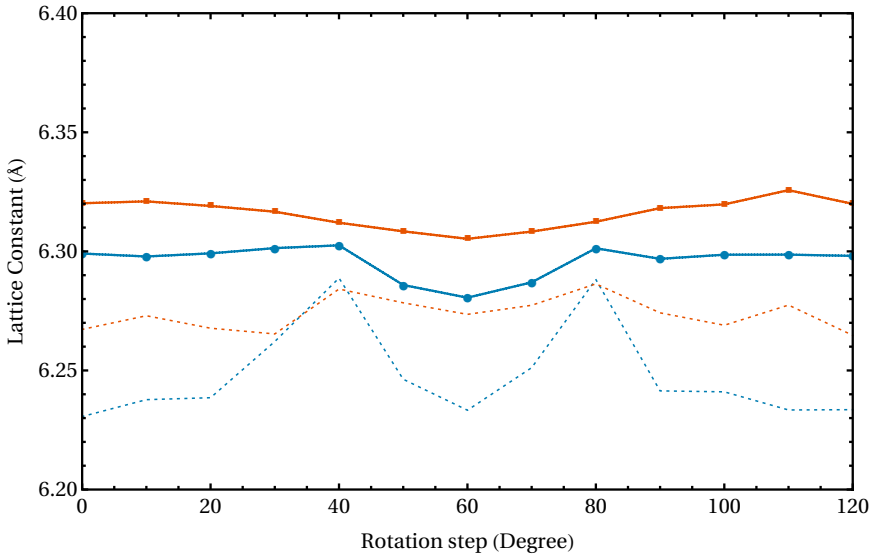

(b) Lattice constant b

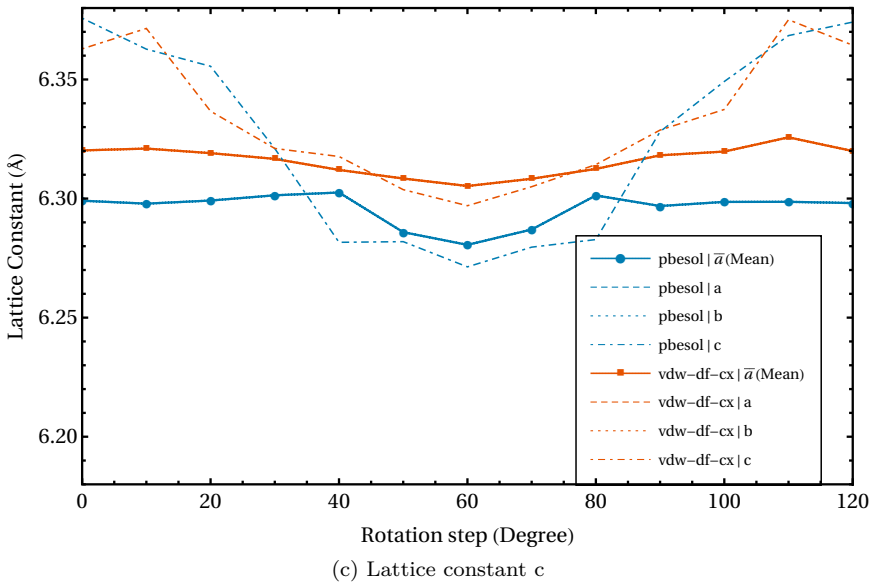

(c) Lattice constant c

Figure 5.5: Lattice Parameter: Lattice Constants by Rotation Step

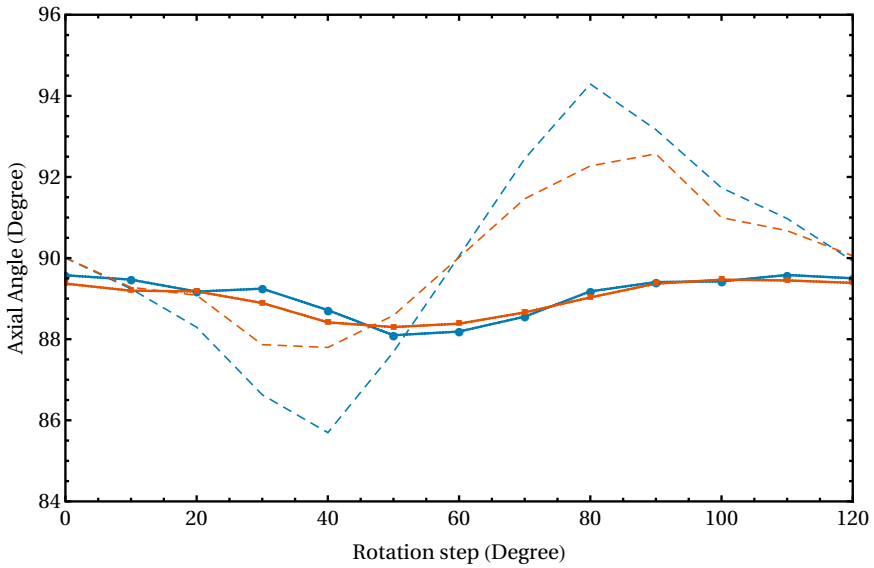

(a) Axial angle α

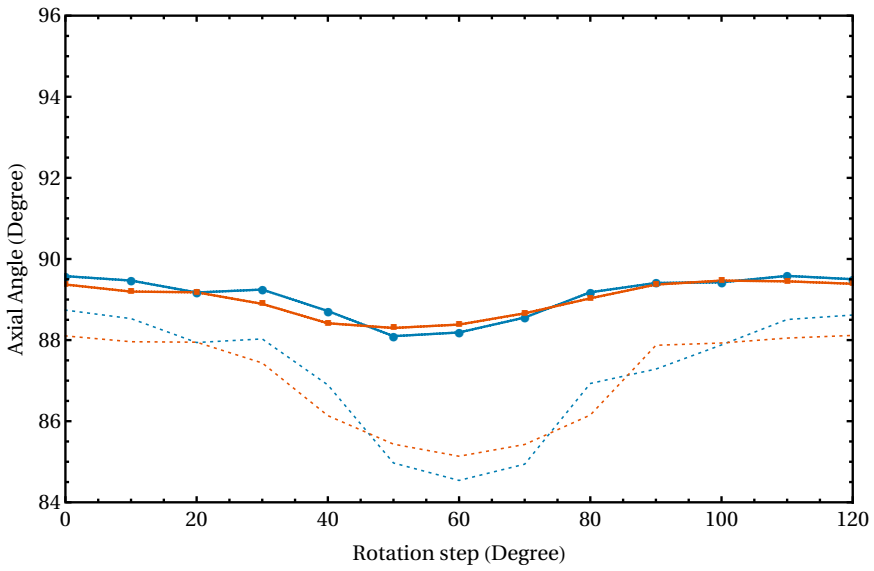

(b) Axial angle β

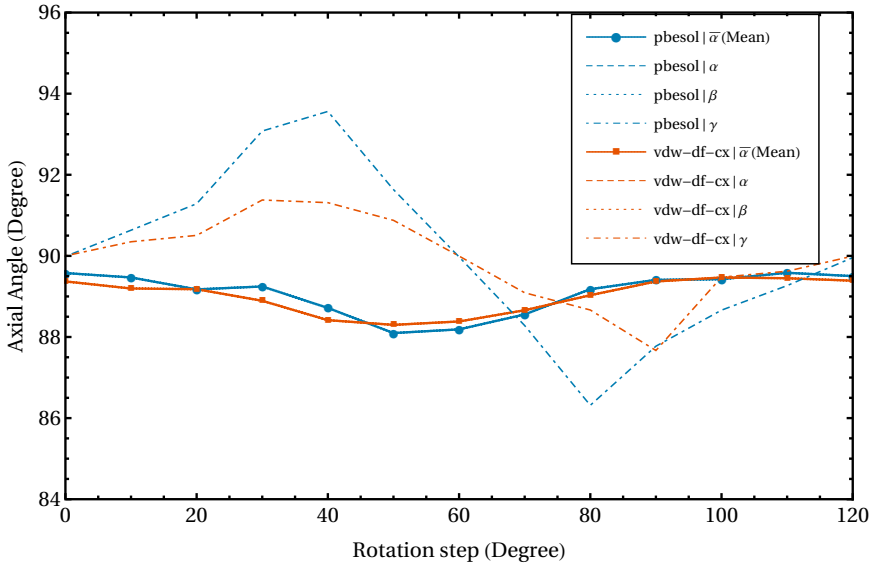

(c) Axial angle γ

Figure 5.6: Lattice Parameter: Axial Angle by Rotation Step

the energy barrier peaks, the lattice constant is minimized.

The variation in axial angle shown in fig.5.6 clearly indicates that, when performing optimization with van der Waals functional, there is less lattice distortion.

5.3.3 Conclusion

In this chapter, we investigate the effects of MA rotation on structural properties of cubic $MAPbI_3$ at ambient pressure. To simulate the rotational dynamics of MA cation using the DFT calculation we have made three assumptions on the rotation schemes. Calculations imply that, if our assumption is valid, the system is less likely to retain its lattice parameter in MA rotation dynamics, and the inorganic network need to adjust to minimize its ground-state energy. Moreover, when performing optimization with van der Waals functional, there is less lattice distortion. Hence, including van der Waals interaction is crucial in $MAPbI_3$ systems and that the system is likely to undergo some equilibrium adjustment in MA rotation.

CHAPTER VI

STRUCTURAL AND ELECTRONIC PROPERTIES OF $MAPbI_3$ AT HIGH PRESSURE

In this chapter, we investigate the effects of pressure to the phase transition observed by experiments. MA orientation and its contribution to electronic properties under pressure were also discussed. Finally, we suggest the possibility of the origin of phase transition under pressure.

6.1 Phase Transition at High Pressure

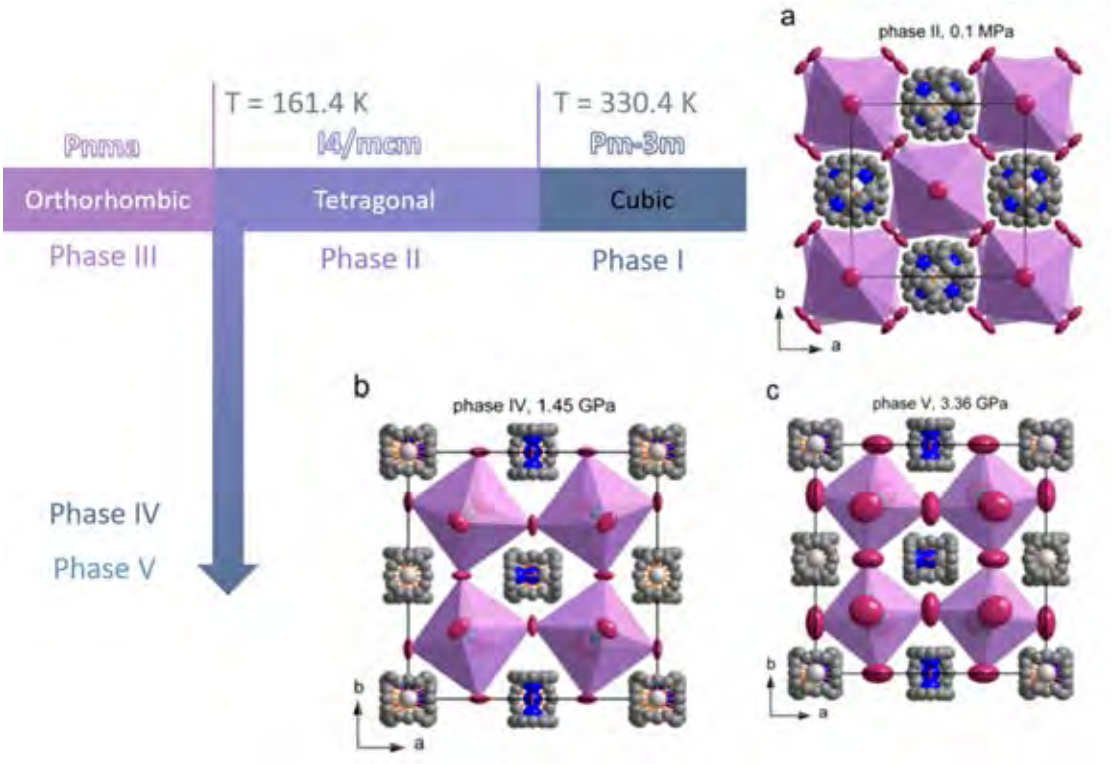

Figure 6.1: Schematic phase transition of $MAPbI_3$. Insets show structures as reported by [2].

Szafranski and Katrusiak have observed $MAPbI_3$ phase transition under high pressure. The ambient pressure phase, which is dubbed as Phase II, has tetragonal structure with space group *I4/mcm*, consistent with those reported by other literatures.[24, 25] When pressurized, the material exhibits changes in optical and structural property, as

shown in Fig. 2.4b. [2] The new phases are called Phase IV and V, with the former exists at lower pressure. Szafranski and Katrusiak have solved the crystal structure to be $Im\bar{3}$ for both high pressure phases, ignoring orientation of MA molecules in the structural refinement processes.

Since the MA orientations are ignored in the structural refinement, we expect that they are related to the change in optical properties. Thus, to better understand the change in optical and structural properties, we suggest 3 models of MA orientation, each models represents the possible extreme cases of maximum and minimum electrical net dipole moments.

6.2 Methodology

In this chapter, we have used the energy cutoff at 90 Ry. The k-point mesh is set to $4 \times 4 \times 4$. These parameters give convergence of the total energy within 2 meV. Other calculation settings were the same as those described in Chapter IV. For the exchange-correlation potential, we have used a generalized gradient approximation (GGA) functional. The scalar relativistic effects are incorporated in the PBEsol functional. The vdW interaction is incorporated in the vdW-DF-cx.

Next, we took the $Im\bar{3}$ structure as suggested by the experiment. [2] Phase IV and V is a $2 \times 2 \times 2$ supercell expansion of the cubic Phase I. The space group gives a guide for the positions of Pb and I atoms. The unit cell contains 8 formula units of $MAPbI_3$, thus there are 8 PbI_6 octahedra, 8 MA molecules, and 8 voids for the MA molecules.

Furthermore, Szafranski and Katrusiak have identified the voids inside the Pb-I mesh, which can be identified into 2 groups as dumbbell and sphere, as shown in Fig. 6.2. The dumbbell has three possible configurations: along [100], [010] and [001] of the simulation cell. They are referred to as x-dumbbell, y-dumbbell and z-dumbbell, respectively. The unknown is the way one can place the MA molecules into those voids. As the MA molecules are a polar molecule (depicted by arrow in 6.4, the arrow head is N and the tail is C), there are 2 possible orientation in one dumbbell void. However, in the simulation cell, there are two x-dumbbell, two y-dumbbell, two z-dumbbell and two sphere voids. Therefore, there are $2^6\times$ (possibility of MA spherical rotation)^2 ways to place the MA inside the voids. See Fig 6.4a for voids inside $Im\bar{3}$ structure.

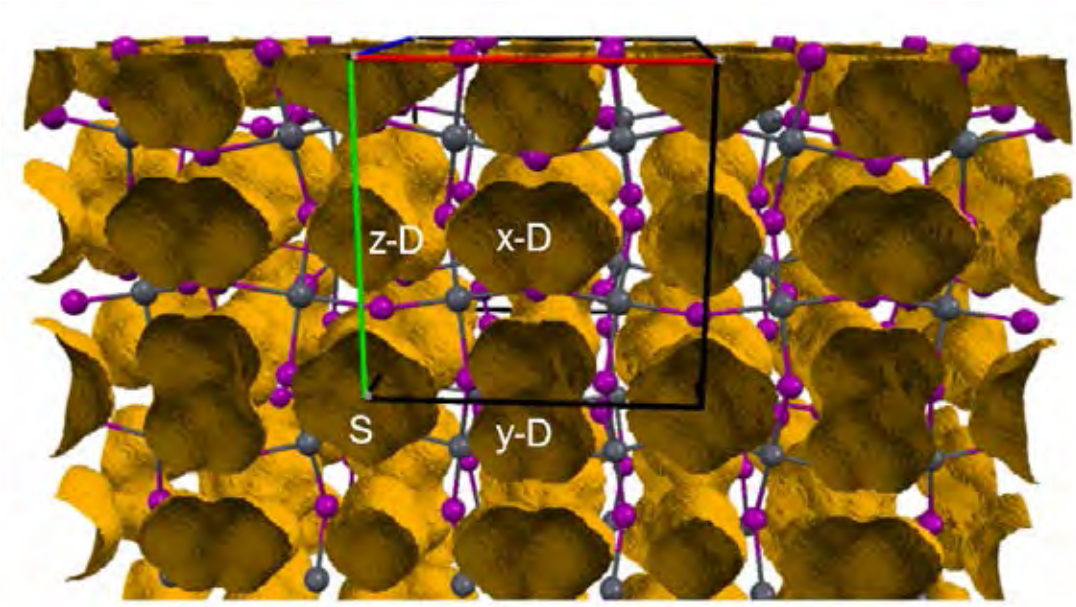

Figure 6.2: Two types of voids in $Im\bar{3}$ space group. S denote sphere void and x-D, y-D, and z-D denote dumbbell voids in their respective orientation. Figure modified from [2] with permission.

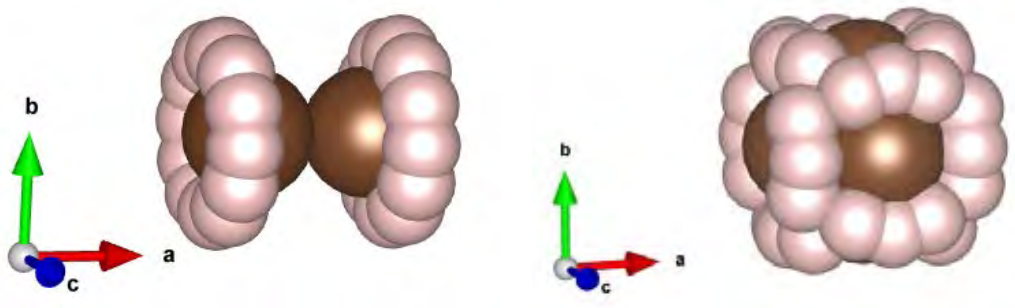

(a) MA in x-dumbbell void

(b) MA in spherical void

Figure 6.3: Possible MA orientations. Brown spheres depict either C or N atom, and white spheres are some possible arrangement of H-atoms

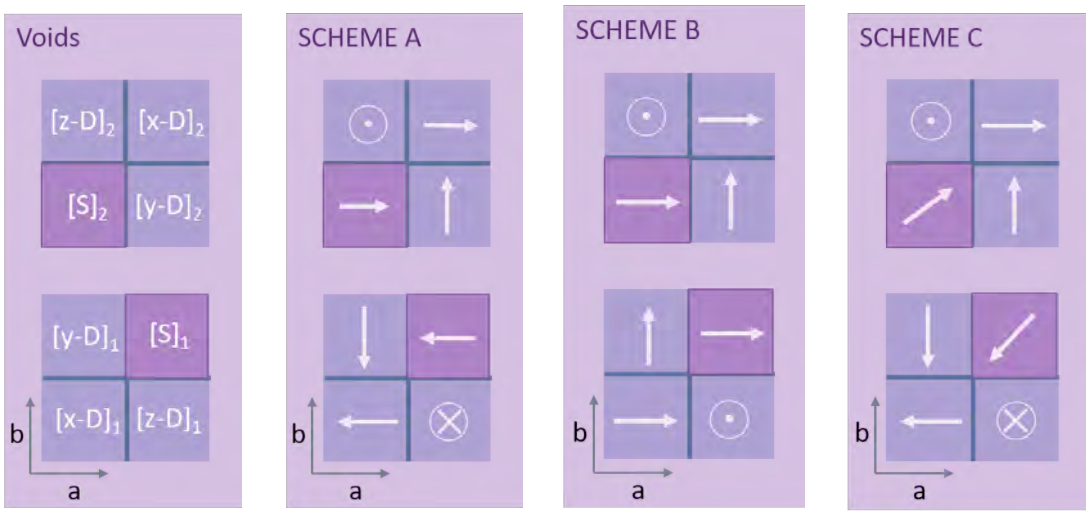

(a) MA as arrow (b) MA of SCHEME A (c) MA of SCHEME B (d) MA of SCHEME C

Figure 6.4: MA orientations that are investigated in this study. We have chosen the orientation that gives highest possible dipole moment (SCHEME B) and two other orientation that give zero net dipole.

To illustrate the orientation of MA molecule, we devised a schematic model as shown in Fig. 6.4. Six blue square are the dumbbell voids and the two dark purple squares are the sphere voids. Arrows are the MA molecules where the head and tail of the arrows are the nitrogen atom and the carbon atom, respectively. The axes show the lattice axes, with the origin of unit cell at the bottom-left of the lower square, with c axis pointing out of paper. Among large number of possibilities, we chose to investigate a number of extreme cases.

SCHEME A in which the MA orientations give the perfect centrosymmetric property and the net dipole moment vanishes.

SCHEME B in which the MA orientations give up the centrosymmetric property and the net dipole moment is maximum.

SCHEME C in which the MA orientations give the perfect centrosymmetric property and the net dipole moment vanishes. The difference between SCHEME A and C is the MA orientations in the spherical voids. The latter is not align along simulation cell basis vectors but in [111] and $[\bar{1}\bar{1}\bar{1}]$ direction.

6.3 Simulation Results

6.3.1 Structural Properties

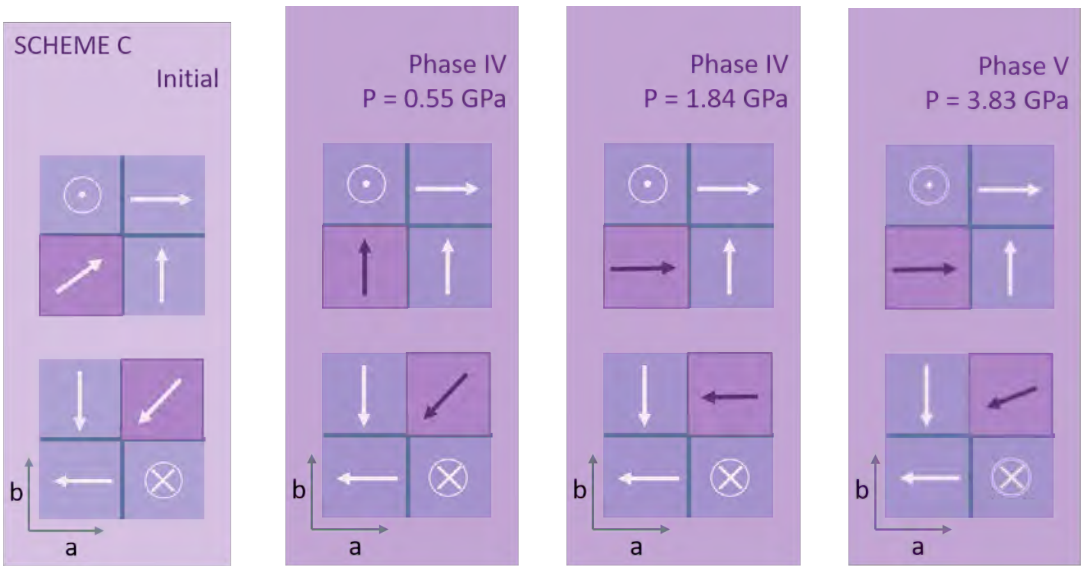

(a) SCHEME C, initial configuration

(b) SCHEME Cr, P = 0.55 GPa

(c) SCHEME Cr, P = 1.84 GPa

(d) SCHEME Cr, P = 3.83 GPa

Figure 6.5: MA orientations that are investigated in this study. (b),(c), and (d) show MA orientation after geometry optimization.

Next, we performed structural optimization starting from scheme C. It is a good starting point because scheme C is not in a minimum energy state. It has a potential to evolve into a lower energy state. The results under pressure are shown schematically in Fig. 6.5. We discovered that at low pressure, 0.55 and 1.84 GPa, the MA molecules in the spherical voids rearrange themselves into a new configuration, scheme Cr, in which the net dipole is finite but not very large compared with that of scheme B. At higher pressure, the relaxed structure resembles that of scheme A.

It is worth noting that the vdW interaction plays a major role here. If we use only the GGA with the relativistic effects, the space group of the simulation cell cannot be held. The simulation cell symmetry can be fixed only by the vdW interaction.

We also plot volume of the unit cell as a function of pressure to show the difference of experimental result (data extracted from Fig.2.4a) and simulation result (SCHEME Cr). The cell volume of our simulation does not show a jump at phase transition pressure, opposed to the experimental result. The lack of change might be due to the simulation

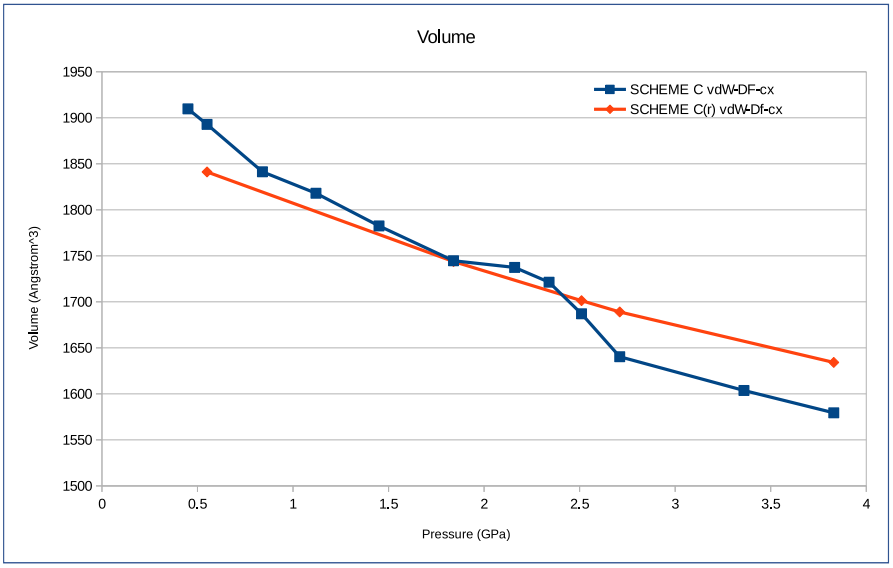

Figure 6.6: Volume of simulation cells, contrasting between SCHEME C and Cr.

limit on including thermal energy. The phase transition might occur at higher pressure, or we have not yet obtained a new phase from geometry optimization at 3.8 GPa.

6.3.2 Ground-state Energy

By using the experimental lattice parameters and direct energy calculations, we found that scheme A gives the lowest energy, and in comparison the energy of A < B < C. Under pressure between 0 - 4 GPa, scheme A is also the lowest energy configuration. Energy per formula unit as a function of pressure is shown in Fig.6.7. We also perform structural optimization on structure of SCHEME C. We discovered that at low pressure, 0.55 and 1.84 GPa, the MA molecules in the spherical voids rearrange themselves into a new configuration (scheme Cr (stands for SCHEME C *relax*)). A plot of energy comparison between scheme C and Cr is also shown in Fig.6.8. Thus, the configuration with the lowest energy is the relaxed structure of SCHEME Cr.

Fig.6.8 shows that simulation cells yield continuous energy change, despite of the rearrangement of MA molecules. Which is likely, since, from Fig. 6.7, the difference in energy of different MA orientation is much less than the energy contribution from volume change.

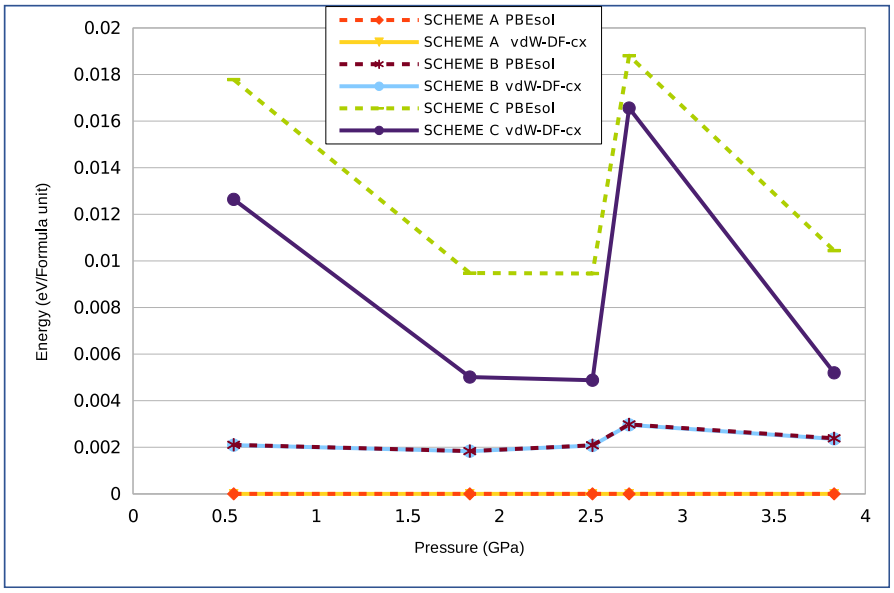

Figure 6.7: Energy of all schemes as a function of pressure. Energy of SCHEME A is subtracted from all other SCHEMES to compare the difference.

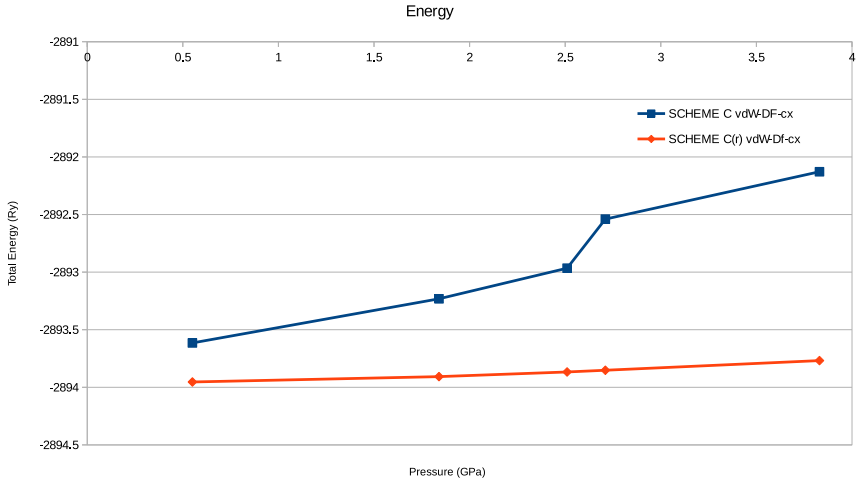

Figure 6.8: Energy of SCHEME Cr compared to scheme C.

6.3.3 Electronic Properties

We have calculated the electronic band structure of some models to experiment with the effect of MA orientation to the electronic properties of phase V. Overall, it can be seen that both simulation on high-pressure phase, Phase IV and V, of $MAPbI_3$ are direct-gap semiconductor; that is, the valence band maximum (VBM) and conduction band minimum (CBM) occur at virtually the same point in the Brillouin zone. Note that all atmospheric phases, cubic Phase I, the tetragonal Phase I and, orthorhombic Phase III, of $MAPbI_3$ are also direct semiconductors.

We calculated the electronic band structure of phase V of MA orientation SCHEME A, SCHEME B, and SCHEME C, with van der Waals interaction included. The result are shown in Fig.6.9, 6.10 and 6.11, respectively. The valence band maxima are minimally affected by the orientation of MA, so is the energy band gap. This is in concordance with our ground-state energy result discussed in section 6.3.2, where the different MA orientation also does not significantly modify the ground-state energy.

We also calculated the band structure of SCHEME Cr using various calculation settings: a) with scalar relativistic GGA approximation with van der Waals correlation functional (as implemented in vdW-DF-cx), b) with full relativistic GGA PBEsol, and c) with scalar relativistic GGA PBEsol, shown in Fig. 6.13, 6.14, and 6.12 respectively. The energy gap is significantly modified by the inclusion of full relativistic effect. The effect narrows energy band from 1.5 eV in Fig.6.13 to 0.5 eV in Fig.6.14. This result is in agreement with previous studies, as reported by [27], since the relativistic effects is significant in heavier atom.

Finally, we calculate the energy band structure of SCHEME Cr at $P = 0.55$ GPa, shown in Fig.6.15, and compare it with energy band structure of SCHEME Cr at $P = 0.55$ GPa, Fig. 6.12. Both results were calculated using vdW-DF-cx correlation functionals. The energy gap of structure at lower pressure is 0.2 eV wider. From this result, we may assume that pressure induces energy band to vary and hence can be used as a method to modify the energy band of $MAPbI_3$.

6.4 Conclusion

We model the phase IV and phase V of $MAPbI_3$ perovskite under high pressure between 0.3 – 4.0 GPa. As suggested by experiment, both phases share the $Im\bar{3}$ space group. However, physical properties, such as Pb-I bond length, Pb-I-Pb bond angle and band gap, exhibit a discontinuity at the transition pressure around 2.5 GPa. We found that the orientations of the MA molecules have large impact on the physical properties. In Phase IV (0.3 - 2.5GPa), the MA molecules in the simulation cell arrange themselves in such a way that the net dipole moment is finite and the simulation cell becomes non-centrosymmetric. Beyond the phase transition ($>$ 2.5GPa), the MA molecules rearrange themselves so that the net dipole moment vanishes and the simulation cell becomes fully centrosymmetric. We discovered that the van der Waals interaction plays a major role in the phase transition as it helps constraint the lattice shape and hence the space group.

From the electronic band structure simulation, we may assume that pressure induces energy band to vary and hence can be used as a method to modify the energy band of $MAPbI_3$.

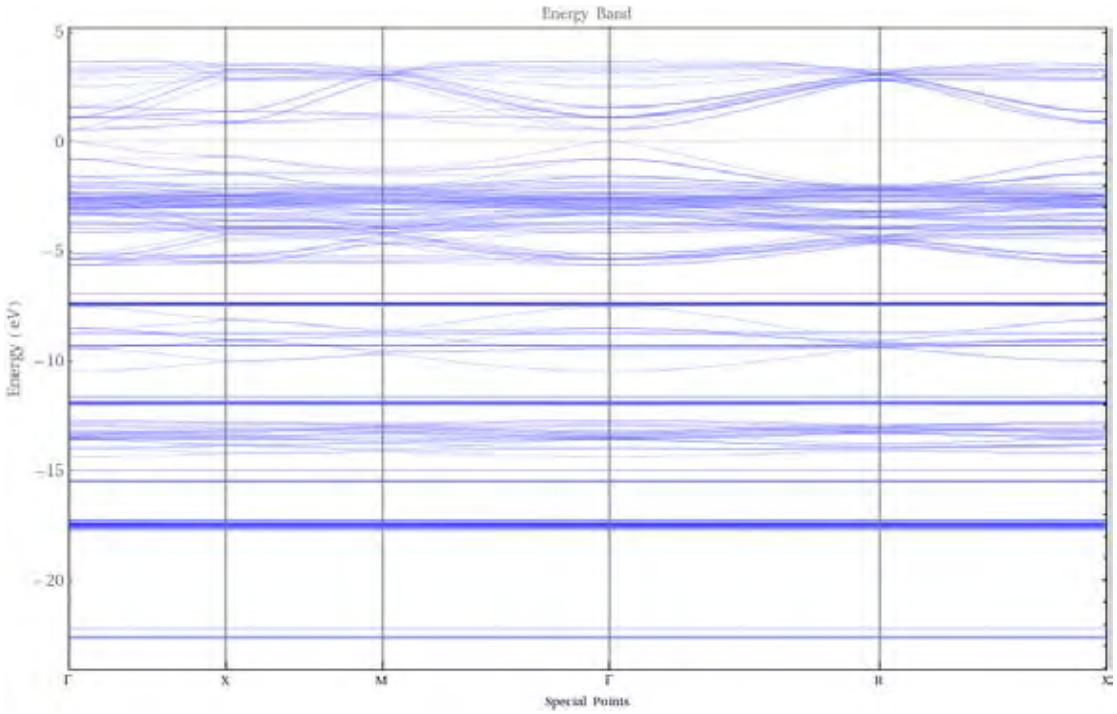

Figure 6.9: Energy band structure of **SCHEME A** at $P = 3.8$ GPa, calculated with vdW-DF-cx correlation functional.

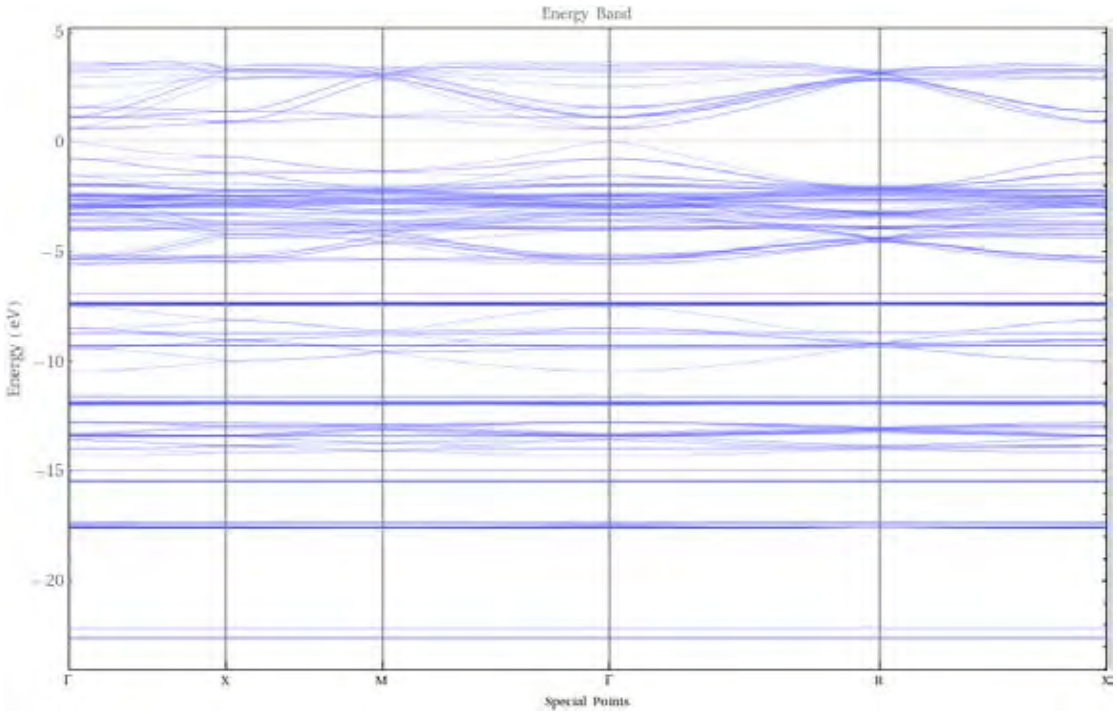

Figure 6.10: Energy band structure of **SCHEME B** at $P = 3.8$ GPa, calculated with vdW-DF-cx correlation functional.

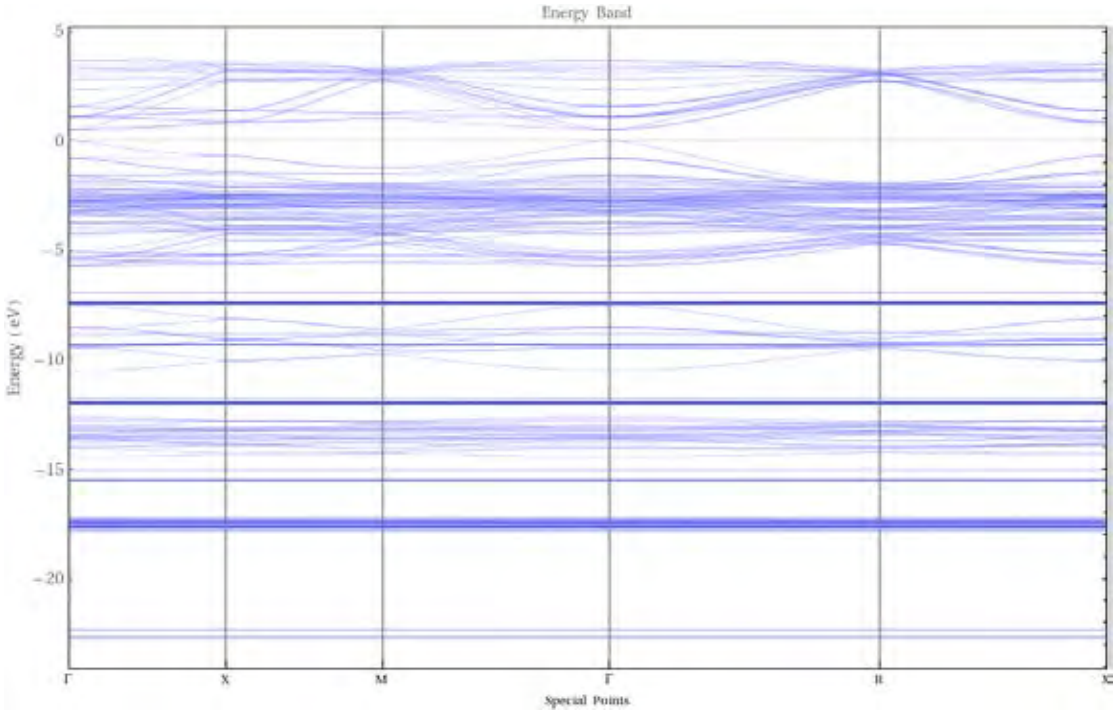

Figure 6.11: Energy band structure of **SCHEME C** at $P = 3.8$ GPa, calculated with vdW-DF-cx correlation functional.

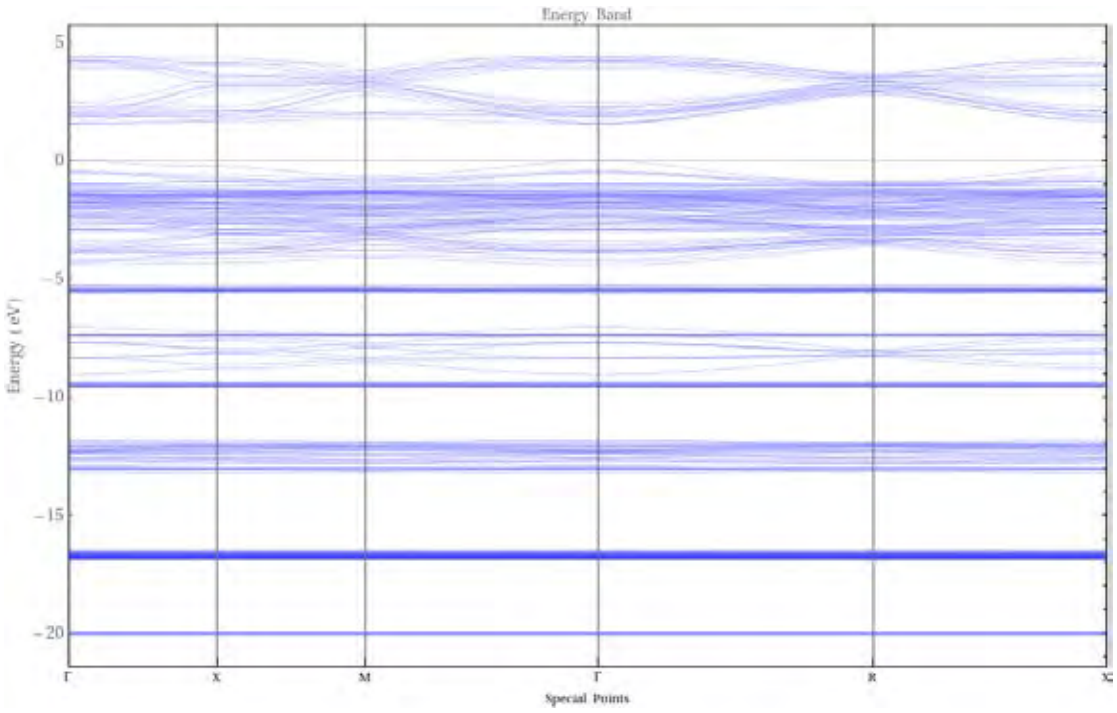

Figure 6.12: Energy band structure of **SCHEME Cr** at $P = 3.8$ GPa, calculated with vdW-DF-cx correlation functional.

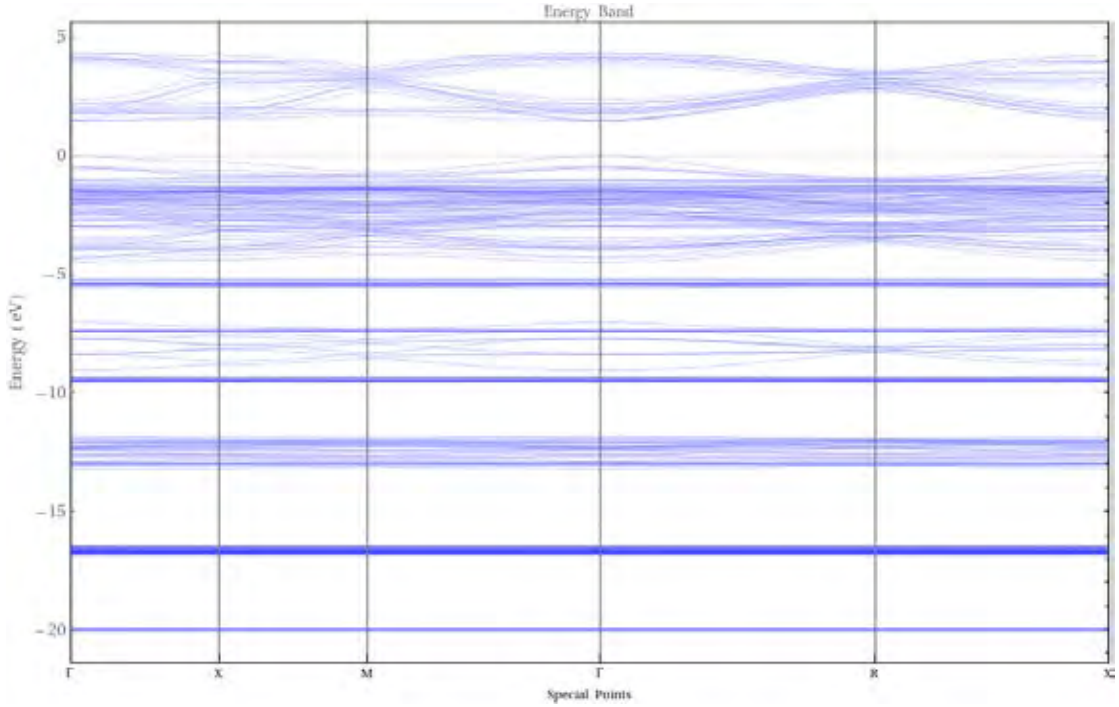

Figure 6.13: Energy band structure of **SCHEME Cr** at $P = 3.8$ GPa, calculated with PBEsol correlation functional, *scalar* relativistic effect included.

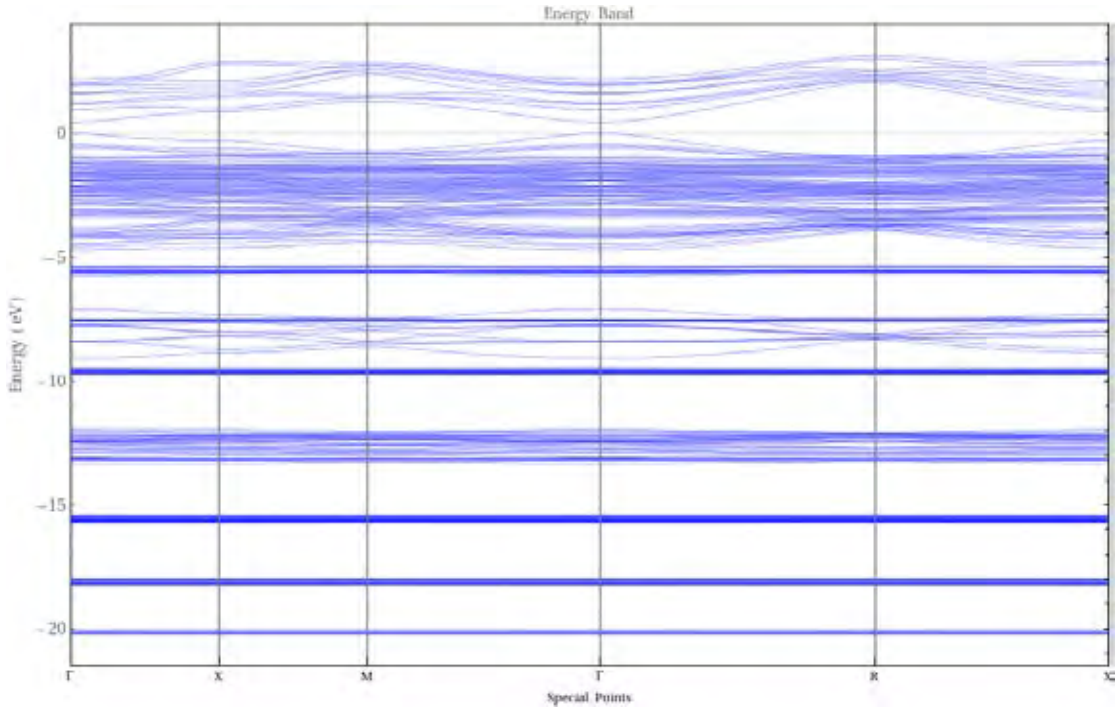

Figure 6.14: Energy band structure of **SCHEME Cr** at $P = 3.8$ GPa, calculated with PBEsol correlation functional, *full* relativistic effect included.

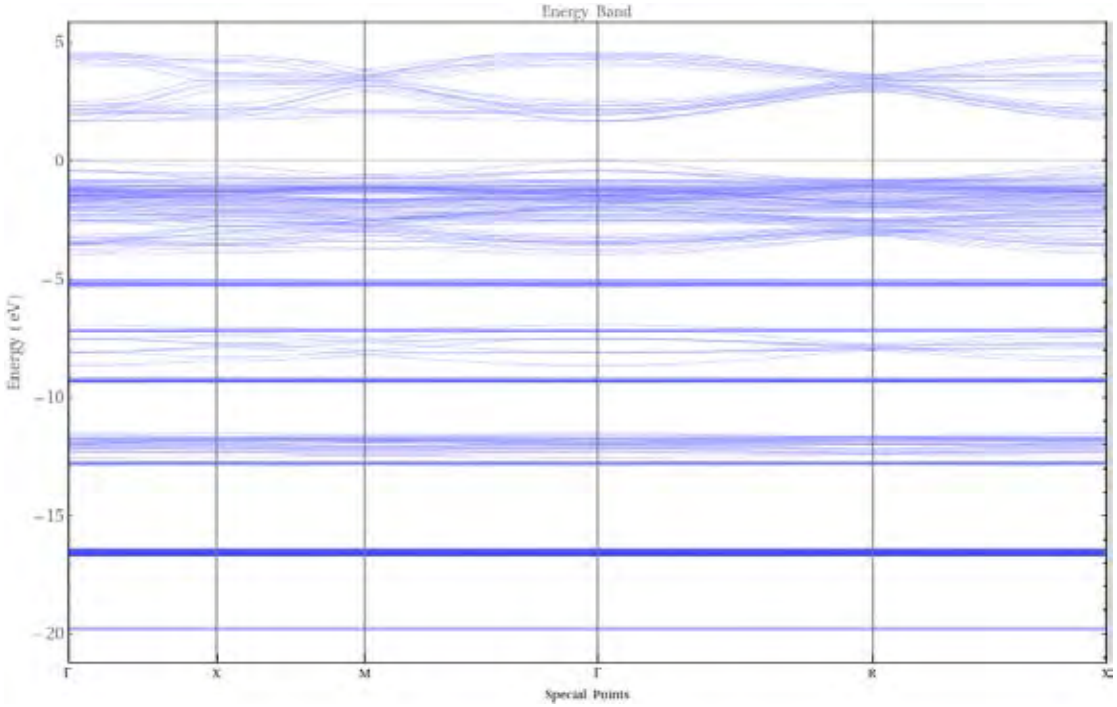

Figure 6.15: Energy band structure of **SCHEME Cr** at $P = 0.55$ GPa, calculated with vdW-DF-cx correlation functional.

CHAPTER VII

THESIS SUMMARY AND CONCLUDING REMARKS

7.1 Thesis Summary

The static DFT calculation is performed with the psuedopotential and plane wave method implemented in Quantum-Espresso package[78]. The disordered C-N axis orientation and the fast on-axis rotation of H-atoms could probably be responsible for the errors in structural parameters. Although the simulations give large error in the C-N and C/N-H bond lengths, the lattice constant and the Pb-I bond length are in good agreement of with those of the experimental results. The latter validates the use of computational model for investigating the local structural and energetic responses to the rotation of H atoms about their C-N axis.

We investigate the effects of MA rotation on structural properties of cubic $MAPbI_3$ at ambient pressure. To simulate the rotational dynamics of MA cation using the DFT calculation we have made three assumptions on the rotation schemes. Calculations imply that, if our assumption is valid, the system is less likely to retain its lattice parameter in MA rotation dynamics, and the inorganic network need to adjust to minimize its ground-state energy. Moreover, when performing optimization with van der Waals functional, there is less lattice distortion. Hence, including van der Waals interaction is crucial in $MAPbI_3$ systems and that the system is likely to undergo some equilibrium adjustment in MA rotation.

The energy barrier of *fix:cell* and *fix:cell+PbI$_3$* are 50% greater than that of *relax* . This implies that, if our assumption is valid, the system is less likely to retain its lattice parameter in MA rotation dynamics, and the inorganic network need to adjust to minimize its ground-state energy.

We model the phase IV and phase V of $MAPbI_3$ perovskite under high pressure between 0.3 – 4.0 GPa. As suggested by experiment, both phases share the $Im\bar{3}$ space group. However, physical properties, such as Pb-I bond length, Pb-I-Pb bond angle and

band gap, exhibit a discontinuity at the transition pressure around 2.5 GPa. We found that the orientations of the MA molecules have large impact on the physical properties. In Phase IV (0.3 - 2.5GPa), the MA molecules in the simulation cell arrange themselves in such a way that the net dipole moment is finite and the simulation cell becomes non-centrosymmetric. Beyond the phase transition (> 2.5GPa), the MA molecules rearrange themselves so that the net dipole moment vanishes and the simulation cell becomes fully centrosymmetric. We discovered that the van der Waals interaction plays a major role in the phase transition as it helps constraint the lattice shape and hence the space group.

It is worth noting that the vdW interaction plays a major role here. The variation in axial angle clearly indicates that, when performing optimization with van der Waals functional, there is less lattice distortion. If we use only the GGA with the relativistic effects, the space group of the simulation cell cannot be held. The simulation cell symmetry can be fixed only by the vdW interaction.

From the electronic band structure simulation, we may assume that pressure induces energy band to vary and hence can be used as a method to modify the energy band of $MAPbI_3$.

7.2 Discussion on Limitations

While we have conducted the research with utmost care, there are limitations that should be addressed.

- Results obtained from density functional theory are subjected to systematic errors arise from the theory itself. All results may not be assume to be valid without careful inspection.
- Density functional theory is most suitable for describing static systems, and is known to be outperformed by other simulation methods. We believe that the results were carefully analyzed, but simulation based on other methods may be compared to evaluate the accuracy of our results.
- Density functional theory calculations do not incorporate the effect of temperature. It is debatable whether the divergence from experimental data is due to temperature or the simulation.

7.3 Concluding Remarks

According to our extensive review, we are the first to employ the density functional theory simulation for studying methylammonium molecule dynamics. We believe that approaches we developed could be extended to give clearer understanding of use for studying perovskite systems in general.

References

1. D. A. Egger, A. M. Rappe, and L. Kronik, "Hybrid Organic-Inorganic Perovskites on the Move," Accounts of Chemical Research, vol. 49, no. 3, pp. 573–581, 2016.

2. M. Szafrański and A. Katrusiak, "Mechanism of Pressure-Induced Phase Transitions, Amorphization, and Absorption-Edge Shift in Photovoltaic Methylammonium Lead Iodide.," The journal of physical chemistry letters, vol. 7, pp. 3458–66, sep 2016.

3. A. M. Glazer, "The classification of tilted octahedra in perovskites," Acta Crystallographica Section B Structural Crystallography and Crystal Chemistry, vol. 28, no. 11, pp. 3384–3392, 1972.

4. C. National Renewable Energy Laboratory, Golden, "Best research-cell efficiencies." `http://www.nrel.gov/ncpv/images/efficiency_chart.jpg`. Accessed July 19, 2016.

5. Y. Yang and J. You, "Make perovskite solar cells stable," Nature, vol. 544, pp. 155–156, apr 2017.

6. J.-P. Correa-Baena, A. Abate, M. Saliba, W. Tress, T. Jesper Jacobsson, M. Grätzel, and A. Hagfeldt, "The rapid evolution of highly efficient perovskite solar cells," Energy Environ. Sci., vol. 10, no. 3, pp. 710–727, 2017.

7. J. S. Manser, M. I. Saidaminov, J. A. Christians, O. M. Bakr, and P. V. Kamat, "Making and Breaking of Lead Halide Perovskites," Accounts of Chemical Research, vol. 49, no. 2, pp. 330–338, 2016.

8. M. Shahbazi and H. Wang, "Progress in research on the stability of organometal perovskite solar cells," Solar Energy, vol. 123, pp. 74–87, 2016.

9. S. Pathak, A. Sepe, A. Sadhanala, F. Deschler, A. Haghighirad, N. Sakai, K. C. Goedel, S. D. Stranks, N. Noel, M. Price, S. Hüttner, N. A. Hawkins, R. H. Friend, U. Steiner, and H. J. Snaith, "Atmospheric influence upon crystallization and electronic disorder and its impact on the photophysical properties of organic-inorganic perovskite solar cells," ACS Nano, vol. 9, no. 3, pp. 2311–2320, 2015.

10. F. Zhang, B. Yang, X. Mao, R. Yang, L. Jiang, Y. Li, J. Xiong, Y. Yang, R. He, W. Deng, and K. Han, "Perovskite CH 3 NH 3 PbI 3– x Br x Single Crystals with Charge-Carrier Lifetimes Exceeding 260 $\mu$$s," $ACSAppliedMaterials\{\&\}Interfaces, vol.$ 9, $p.$ $acsami.7b01696, may 2017.$

11. G. Grancini, C. Roldán-Carmona, I. Zimmermann, E. Mosconi, X. Lee, D. Martineau, S. Narbey, F. Oswald, F. De Angelis, M. Graetzel, and M. K. Nazeeruddin, "One-Year stable perovskite solar cells by 2D/3D interface engineering," Nature Communications, vol. 8, p. 15684, jun 2017.

12. Q. Wang, B. Chen, Y. Liu, Y. Deng, Y. Bai, Q. Dong, and J. Huang, "Scaling behavior of moisture-induced grain degradation in polycrystalline hybrid perovskite thin films," Energy Environ. Sci., vol. 10, no. 2, pp. 516–522, 2017.

13. B. Hwang and J.-s. Lee, "Hybrid Organic-Inorganic Perovskite Memory with Long-Term Stability in Air," Scientific Reports, vol. 7, p. 673, dec 2017.

14. F. Bella, G. Griffini, J.-P. Correa-Baena, G. Saracco, M. Gratzel, A. Hagfeldt, S. Turri, and C. Gerbaldi, "Improving efficiency and stability of perovskite solar cells with photocurable fluoropolymers," Science, vol. 354, no. 6309, pp. 203–206, 2016.

15. M. Saliba, T. Matsui, K. Domanski, J.-Y. Seo, A. Ummadisingu, S. M. Zakeeruddin, J.-P. Correa-Baena, W. R. Tress, A. Abate, A. Hagfeldt, and M. Gratzel, "Incorporation of rubidium cations into perovskite solar cells improves photovoltaic performance," Science, vol. 354, no. 6309, pp. 206–209, 2016.

16. H. Tsai, W. Nie, J.-C. Blancon, C. C. Stoumpos, R. Asadpour, B. Harutyunyan, A. J. Neukirch, R. Verduzco, J. J. Crochet, S. Tretiak, L. Pedesseau, J. Even, M. A. Alam, G. Gupta, J. Lou, P. M. Ajayan, M. J. Bedzyk, M. G. Kanatzidis, and A. D. Mohite, "High-efficiency two-dimensional Ruddlesden–Popper perovskite solar cells," Nature, vol. 536, pp. 312–316, jul 2016.

17. A. L. Montero-Alejo, E. Menéndez-Proupin, D. Hidalgo-Rojas, P. Palacios, P. Wahnón, and J. C. Conesa, "Modeling of Thermal Effect on the Electronic Properties of Photovoltaic Perovskite CH 3 NH 3 PbI 3 : The Case of Tetragonal Phase," The Journal of Physical Chemistry C, vol. 120, p. acs.jpcc.6b01013, apr 2016.

18. N. K. Kumawat, M. N. Tripathi, U. Waghmare, and D. Kabra, "Structural, Optical, and Electronic Properties of Wide Bandgap Perovskites: Experimental and Theoret-

ical Investigations," The Journal of Physical Chemistry A, vol. 120, pp. 3917–3923, jun 2016.

19. S. Jiang, Y. Fang, R. Li, H. Xiao, J. Crowley, C. Wang, T. J. White, W. A. Goddard, Z. Wang, T. Baikie, and J. Fang, "Pressure-Dependent Polymorphism and Band-Gap Tuning of Methylammonium Lead Iodide Perovskite," Angewandte Chemie International Edition, vol. 55, pp. 6540–6544, may 2016.

20. Y. Jiao, F. Ma, H. Wang, J. Bell, and A. Du, "Strain Mediated Bandgap Reduction, Light Spectrum Broadening, and Carrier Mobility Enhancement of Methylammonium Lead/Tin Iodide Perovskites," Particle & Particle Systems Characterization, p. 1600288, 2017.

21. G. Liu, L. Kong, J. Gong, W. Yang, H.-k. Mao, Q. Hu, Z. Liu, R. D. Schaller, D. Zhang, and T. Xu, "Pressure-Induced Bandgap Optimization in Lead-Based Perovskites with Prolonged Carrier Lifetime and Ambient Retainability," Advanced Functional Materials, vol. 201604208, no. December, pp. 1–8, 2016.

22. M. I. Aroyo, ed., International Tables for Crystallography, vol. A. Chester, England: International Union of Crystallography, dec 2016.

23. `https://en.wikipedia.org/wiki/`.

24. M. T. Weller, O. J. Weber, P. F. Henry, A. M. Di Pumpo, and T. C. Hansen, "Complete structure and cation orientation in the perovskite photovoltaic methylammonium lead iodide between 100 and 352 K," Chem. Commun., vol. 51, no. 20, pp. 4180–4183, 2015.

25. N. Onoda-Yamamuro, T. Matsuo, and H. Suga, "Calorimetric and IR spectroscopic studies of phase transitions in methylammonium trihalogenoplumbates (II)†," Journal of Physics and Chemistry of Solids, vol. 51, pp. 1383–1395, jan 1990.

26. M. A. Green, A. Ho-Baillie, and H. J. Snaith, "The emergence of perovskite solar cells," Nature Photonics, vol. 8, no. 7, pp. 506–514, 2014.

27. T. M. Brenner, D. A. Egger, L. Kronik, G. Hodes, and D. Cahen, "Hybrid organic—inorganic perovskites: low-cost semiconductors with intriguing charge-transport properties," Nature Reviews Materials, vol. 1, p. 15007, jan 2016.

28. F. Zheng, D. Saldana-Greco, S. Liu, and A. M. Rappe, "Material Innovation in Advancing Organometal Halide Perovskite Functionality," Journal of Physical Chemistry Letters, vol. 6, no. 23, pp. 4862–4872, 2015.

29. J. Even, L. Pedesseau, C. Katan, M. Kepenekian, J. Lauret, D. Sapori, and E. Deleporte, "Solid-state physics perspective on hybrid perovskite semiconductors.," J. Phys. Chem. C., vol. 119, pp. 1016–10177, 2015.

30. A. Kojima, K. Teshima, Y. Shirai, and T. Miyasaka, "Organometal halide perovskites as visible-light sensitizers for photovoltaic cells," Journal of the American Chemical Society, vol. 131, no. 17, pp. 6050–6051, 2009.

31. G. Hodes, "Perovskite-based solar cells.," Science (New York, N.Y.), vol. 342, no. 2013, pp. 317–8, 2013.

32. T. Baikie, Y. Fang, J. M. Kadro, M. Schreyer, F. Wei, S. G. Mhaisalkar, M. Gratzel, and T. J. White, "Synthesis and crystal chemistry of the hybrid perovskite (CH3NH3)PbI3 for solid-state sensitised solar cell applications," Journal of Materials Chemistry A, vol. 1, no. 18, p. 5628, 2013.

33. Y. Wang, T. Gould, J. F. Dobson, H. Zhang, H. Yang, X. Yao, and H. Zhao, "Density functional theory analysis of structural and electronic properties of orthorhombic perovskite CH 3 NH 3 PbI 3," Phys. Chem. Chem. Phys., vol. 16, no. 4, pp. 1424–1429, 2014.

34. F. Brivio, J. M. Frost, J. M. Skelton, A. J. Jackson, O. J. Weber, M. T. Weller, A. R. Go??i, A. M. A. M. A. M. A. Leguy, P. R. F. Barnes, A. Walsh, A. R. Goñi, A. M. A. M. A. M. A. Leguy, P. R. F. Barnes, and A. Walsh, "Lattice dynamics and vibrational spectra of the orthorhombic, tetragonal, and cubic phases of methylammonium lead iodide," Physical Review B - Condensed Matter and Materials Physics, vol. 92, no. 14, pp. 1–8, 2015.

35. J. M. Frost, K. T. Butler, and A. Walsh, "Molecular ferroelectric contributions to anomalous hysteresis in hybrid perovskite solar cells," APL Mater., vol. 2, p. 081506, 2014.

36. J. M. Frost, K. T. Butler, F. Brivio, C. H. Hendon, M. V. Schilfgaarde, and A. Walsh, "Atomistic origins of high-performance in hybrid halide perovskite solar cells," Nano Lett., vol. 14, pp. 2584–2590, 2014.

37. T. Baikie, N. S. Barrow, Y. Fang, P. J. Keenan, P. R. Slater, R. O. Piltz, M. Gutmann, S. G. Mhaisalkar, and T. J. White, "A combined single crystal neutron/X-ray diffraction and solid-state nuclear magnetic resonance study of the hybrid perovskites CH ₃ NH ₃ PbX ₃ (X = I, Br and Cl)," J. Mater. Chem. A, vol. 3, no. 17, pp. 9298–9307, 2015.

38. E. Mosconi, C. Quarti, T. Ivanovska, G. Ruani, and F. De Angelis, "Structural and electronic properties of organo-halide lead perovskites: a combined IR-spectroscopy and ab initio molecular dynamics investigation," Physical Chemistry Chemical Physics, vol. 16, no. 30, p. 16137, 2014.

39. C. Quarti, E. Mosconi, and F. De Angelis, "Structural and electronic properties of organo-halide hybrid perovskites from ab initio molecular dynamics," Phys. Chem. Chem. Phys., vol. 17, no. 14, pp. 9394–9409, 2015.

40. K. P. Ong, T. W. Goh, Q. Xu, and A. Huan, "Structural Evolution in Methylammonium Lead Iodide CH 3 NH 3 PbI 3," The Journal of Physical Chemistry A, vol. 119, pp. 11033–11038, nov 2015.

41. I. Deretzis, B. N. D. Mauro, A. Alberti, G. Pellegrino, E. Smecca, and A. L. Magna, "Spontaneous bidirectional ordering of $CH_3NH_3PbI_3$ in lead iodide perovskites at room temperature: The origins of the tetragonal phase," Sci. Rep., vol. 6, p. 24443, 2016.

42. A. M. A. Leguy, J. M. Frost, A. P. McMahon, V. G. Sakai, W. Kochelmann, C. Law, X. Li, F. Foglia, A. Walsh, B. C. O'Regan, J. Nelson, J. T. Cabral, and P. R. F. Barnes, "The dynamics of methylammonium ions in hybrid organic-inorganic perovskite solar cells.," Nature communications, vol. 6, no. May, p. 7124, 2015.

43. M. A. Carignano, A. Kachmar, and J. Hutter, "Thermal Effects on CH 3 NH 3 PbI 3 Perovskite from Ab Initio Molecular Dynamics Simulations," The Journal of Physical Chemistry C, vol. 119, no. 17, pp. 8991–8997, 2015.

44. T. Chen, B. J. Foley, B. Ipek, M. Tyagi, J. R. D. Copley, C. M. Brown, J. J. Choi, and S.-H. Lee, "Rotational dynamics of organic cations in the CH 3 NH 3 PbI 3 perovskite," Phys. Chem. Chem. Phys., vol. 17, no. 46, pp. 31278–31286, 2015.

45. J. Li and P. Rinke, "Atomic structure of metal-halide perovskites from first principles: The chicken-and-egg paradox of the organic-inorganic interaction," Physical Review B - Condensed Matter and Materials Physics, vol. 94, no. 4, pp. 1–4, 2016.

46. C. Motta, F. El-Mellouhi, and S. Sanvito, "Exploring the cation dynamics in lead bromide hybrid perovskites," Phys. Rev. B., vol. 93, p. 235412, 2016.

47. J. H. Lee, N. C. Bristowe, P. D. Bristowe, and A. K. Cheetham, "Role of hydrogen-bonding and its interplay with octahedral tilting in $CH_3NH_3PbI_3$," Chem. Commun., vol. 51, pp. 6434–6437, 2015.

48. J. W. Lee, H. S. Kim, and N. G. Park, "Lewis Acid-Base Adduct Approach for High Efficiency Perovskite Solar Cells," Accounts of Chemical Research, vol. 49, no. 2, pp. 311–319, 2016.

49. T. Hata, G. Giorgi, and K. Yamashita, "The effects of organic-inorganic interactions on thermal transport properties of $CH_3NH_3PbI_3$," Nano Lett., vol. 16, pp. 2749–2753, 2016.

50. K. Berland and P. hylgaard, "Exchange functional that tests the robustness of plasmon description of the van der waals density functional," Phys. Rev. B., vol. 89, p. 035412, 2014.

51. J. klimeš, D. R. Bowler, and A. Michaelides, "van der waals density functional applied to solids," Phys. Rev. B., vol. 83, p. 195131, 2011.

52. J. P. P. Ramalho, J. R. B. Gomes, and F. Illas, "Accounting for van der waals interactions between adsorbates and surfaces in density functional theory based calculations; selected examples," RSC Adv., vol. 3, pp. 13085–13100, 2013.

53. L. Kong, G. Liu, J. Gong, Q. Hu, R. D. Schaller, P. Dera, D. Zhang, Z. Liu, W. Yang, K. Zhu, Y. Tang, C. Wang, S.-H. Wei, T. Xu, and H.-k. Mao, "Simultaneous band-gap narrowing and carrier-lifetime prolongation of organic–inorganic trihalide perovskites," Proceedings of the National Academy of Sciences, vol. 113, pp. 8910–8915, aug 2016.

54. M. Born and R. Oppenheimer, "Zur quantentheorie der molekeln," Annalen der Physik, vol. 389, no. 20, pp. 457–484, 1927.

55. D. R. Hartree, "The wave mechanics of an atom with a non-coulomb central field. part i. theory and methods," in Mathematical Proceedings of the Cambridge Philosophical Society, vol. 24, pp. 89–110, Cambridge Univ Press, 1928.

56. V. Fock, "Näherungsmethode zur lösung des quantenmechanischen mehrkörperproblems," Zeitschrift für Physik A Hadrons and Nuclei, vol. 61, no. 1, pp. 126–148, 1930.

57. P. Hohenberg and W. Kohn, "Inhomogeneous electron gas," Physical review, vol. 136, no. 3B, p. B864, 1964.

58. L. H. Thomas, "The calculation of atomic fields," in Mathematical Proceedings of the Cambridge Philosophical Society, vol. 23, pp. 542–548, Cambridge Univ Press, 1927.

59. E. Fermi, "Statistical method to determine some properties of atoms," Rend. Accad. Naz. Lincei, vol. 6, pp. 602–607, 1927.

60. E. Fermi, "Eine statistische methode zur bestimmung einiger eigenschaften des atoms und ihre anwendung auf die theorie des periodischen systems der elemente," Zeitschrift für Physik, vol. 48, no. 1-2, pp. 73–79, 1928.

61. C. Kittel, Introduction to solid state physics. Wiley, 2005.

62. N. W. Ashcroft and N. D. Mermin, "Solid state physics," 1976.

63. C. Herring, "A new method for calculating wave functions in crystals," Physical Review, vol. 57, no. 12, p. 1169, 1940.

64. J. C. Phillips and L. Kleinman, "New method for calculating wave functions in crystals and molecules," Physical Review, vol. 116, no. 2, p. 287, 1959.

65. D. Hamann, M. Schlüter, and C. Chiang, "Norm-conserving pseudopotentials," Physical Review Letters, vol. 43, no. 20, p. 1494, 1979.

66. D. Vanderbilt, "Soft self-consistent pseudopotentials in a generalized eigenvalue formalism," Physical Review B, vol. 41, no. 11, p. 7892, 1990.

67. H. J. Monkhorst and J. D. Pack, "Special points for brillouin-zone integrations," Physical review B, vol. 13, no. 12, p. 5188, 1976.

68. B. G. Pfrommer, M. Côté, S. G. Louie, and M. L. Cohen, "Relaxation of crystals with the quasi-newton method," Journal of Computational Physics, vol. 131, no. 1, pp. 233–240, 1997.

69. http://github.com/WMD-Bath/Hybrid-perovskites.

70. R. Sabatini, T. Gorni, and S. de Gironcoli, "Nonlocal van der waals density functional made simple and efficient," Phys. Rev. B, vol. 87, p. 041108, Jan 2013.

71. M. Dion, H. Rydberg, E. Schroder, D. C. Langreth, and B. I. Lundqvist, "Van der waals density functional for general geometries," Phys. Rev. Lett., vol. 92, p. 246401, 2004.

72. T. Thonhauser, S. Zuluaga, C. A. Arter, K. Berland, E. Schröder, and P. Hyldgaard, "Spin signature of nonlocal correlation binding in metal-organic frameworks," Phys. Rev. Lett., vol. 115, p. 136402, Sep 2015.

73. K. Lee, E. D. Murray, L. Kong, B. I. Lundqvist, and D. C. Langreth, "Higher-accuracy van der waals density functional," Phys. Rev. B, vol. 82, p. 081101, Aug 2010.

74. J. c. v. Klimeš, D. R. Bowler, and A. Michaelides, "Van der waals density functionals applied to solids," Phys. Rev. B, vol. 83, p. 195131, May 2011.

75. K. Berland and P. Hyldgaard, "Exchange functional that tests the robustness of the plasmon description of the van der waals density functional," Phys. Rev. B, vol. 89, p. 035412, Jan 2014.

76. J. P. Perdew, K. Burke, and M. Ernzerhof, "Generalized gradient approximation made simple," Phys. Rev. Lett., vol. 77, pp. 3865–3868, Oct 1996.

77. J. P. Perdew, A. Ruzsinszky, G. I. Csonka, O. A. Vydrov, G. E. Scuseria, L. A. Constantin, X. Zhou, and K. Burke, "Restoring the density-gradient expansion for exchange in solids and surfaces," Phys. Rev. Lett., vol. 100, p. 136406, Apr 2008.

78. P. Giannozzi, S. Baroni, N. Bonini, M. Calandra, R. Car, C. Cavazzoni, D. Ceresoli, G. L. Chiarotti, M. Cococcioni, I. Dabo, A. D. Corso, S. de Gironcoli, S. Fabris, G. Fratesi, R. Gebauer, U. Gerstmann, C. Gougoussis, A. Kokalj, M. Lazzeri, L. Martin-Samos, N. Marzari, F. Mauri, R. Mazzarello, S. Paolini, A. Pasquarello, L. Paulatto, C. Sbraccia, S. Scandolo, G. Sclauzero, A. P. Seitsonen, A. Smogunov, P. Umari, and R. M. Wentzcovitch, "Quantum espresso: a modular and open-source software project for quantum simulations of materials," Journal of Physics: Condensed Matter, vol. 21, no. 39, p. 395502, 2009.

79. http://www.qe-forge.org/gf/project/pslibrary/.

80. P. Umari, E. Mosconi, and F. De Angelis, "Relativistic GW calculations on CH3NH3PbI3 and CH3NH3SnI3 perovskites for solar cell applications.," Scientific Reports, vol. 4, p. 4467, 2014.

81. H. J. Monkhorst and J. D. Pack, "Special points for brillouin-zone integrations," Phys. Rev. B, vol. 13, pp. 5188–5192, Jun 1976.

APPENDICES

APPENDIX A

INPUT STRUCTURAL PARAMETERS

Cell Parameters (in Å)

Cell Parameters	X	Y	Z
6.290877638	-0.000014545	0.000243067	
0.001528808	6.230653561	-0.000008544	
0.140025692	-0.000374861	6.374202938	

Atomic Position (in fractional coordinates)

Atomic Position	X	Y	Z
C	0.893745075	0.999816924	0.457735243
N	0.109195427	0.000006777	0.547821880
H	0.910141919	0.999641910	0.285636727
H	0.808596364	0.144819585	0.511081067
H	0.808805138	0.854837436	0.511351171
H	0.196424184	0.135963615	0.501449807
H	0.196566282	0.863996219	0.501717042
H	0.106371216	0.000186827	0.711468178
Pb	0.444917804	0.499978318	0.977661853
I	0.409453170	0.499980685	0.475123079
I	0.399225353	0.999960916	0.023634097
I	0.932337076	0.499993728	0.922452790

Table A.1: Input atomic position of cubic $MAPbI_3$ for *relax*

Cell Parameters (in Å)

Cell Parameters	X	Y	Z
11.645700	0	0	
0	11.645700	0	
0	0	11.645700	

Atomic Position (in fractional coordinates)

Atomic Position	X	Y	Z
Pb	0.250000	0.250000	0.250000
I	0.000000	0.223300	0.272200
I	0.272200	0.000000	0.223300
I	0.223300	0.272200	0.000000

C	0.937300	0.000000	0.000000
N	0.062700	0.000000	0.000000
H	0.912500	0.038700	0.067100
H	0.912500	0.038700	0.932900
H	0.922500	0.912500	0.000000
H	0.087500	0.961300	0.067100
H	0.077500	0.087500	0.000000
H	0.087500	0.961300	0.932900
Pb	0.750000	0.250000	0.250000
I	0.500000	0.276700	0.227800
I	0.727800	0.000000	0.223300
I	0.776700	0.272200	0.000000
C	0.500000	0.937300	0.000000
N	0.500000	0.062700	0.000000
H	0.538000	0.910000	0.065800
H	0.424000	0.910000	0.000000
H	0.538000	0.910000	0.934200
H	0.462000	0.090000	0.065800
H	0.462000	0.090000	0.934200
H	0.576000	0.090000	0.000000
Pb	0.250000	0.750000	0.250000
I	0.000000	0.776700	0.272200
I	0.227800	0.500000	0.276700
I	0.223300	0.727800	0.000000
C	0.000000	0.500000	0.937300
N	0.000000	0.500000	0.062700
H	0.934200	0.538000	0.910000
H	0.065800	0.538000	0.910000
H	0.000000	0.424000	0.910000
H	0.934200	0.462000	0.090000
H	0.000000	0.576000	0.090000
H	0.065800	0.462000	0.090000
Pb	0.750000	0.750000	0.250000

I	0.500000	0.723300	0.227800
I	0.772200	0.500000	0.276700
I	0.776700	0.727800	0.000000
C	0.437300	0.500000	0.000000
N	0.562700	0.500000	0.000000
H	0.410000	0.565800	0.038000
H	0.410000	0.434200	0.038000
H	0.410000	0.500000	0.924000
H	0.590000	0.500000	0.076000
H	0.590000	0.434200	0.962000
H	0.590000	0.565800	0.962000
Pb	0.250000	0.250000	0.750000
I	0.000000	0.223300	0.727800
I	0.272200	0.000000	0.776700
I	0.276700	0.227800	0.500000
C	0.062700	0.000000	0.500000
N	0.937300	0.000000	0.500000
H	0.090000	0.000000	0.576000
H	0.090000	0.934200	0.462000
H	0.090000	0.065800	0.462000
H	0.910000	0.065800	0.538000
H	0.910000	0.934200	0.538000
H	0.910000	0.000000	0.424000
Pb	0.750000	0.250000	0.750000
I	0.500000	0.276700	0.772200
I	0.727800	0.000000	0.776700
I	0.723300	0.227800	0.500000
C	0.500000	0.000000	0.562700
N	0.500000	0.000000	0.437300
H	0.500000	0.076000	0.590000
H	0.565800	0.962000	0.590000
H	0.434200	0.962000	0.590000
H	0.434200	0.038000	0.410000

H	0.565800	0.038000	0.410000
H	0.500000	0.924000	0.410000
Pb	0.250000	0.750000	0.750000
I	0.000000	0.776700	0.727800
I	0.227800	0.500000	0.723300
I	0.276700	0.772200	0.500000
C	0.000000	0.562700	0.500000
N	0.000000	0.437300	0.500000
H	0.962000	0.590000	0.565800
H	0.076000	0.590000	0.500000
H	0.962000	0.590000	0.434200
H	0.038000	0.410000	0.565800
H	0.038000	0.410000	0.434200
H	0.924000	0.410000	0.500000
Pb	0.750000	0.750000	0.750000
I	0.500000	0.723300	0.772200
I	0.772200	0.500000	0.723300
I	0.723300	0.772200	0.500000
C	0.562700	0.500000	0.500000
N	0.437300	0.500000	0.500000
H	0.587500	0.461300	0.567100
H	0.577500	0.587500	0.500000
H	0.587500	0.461300	0.432900
H	0.412500	0.538700	0.567100
H	0.412500	0.538700	0.432900
H	0.422500	0.412500	0.500000

Table A.4: Input atomic position of Phase V $MAPbI_3$

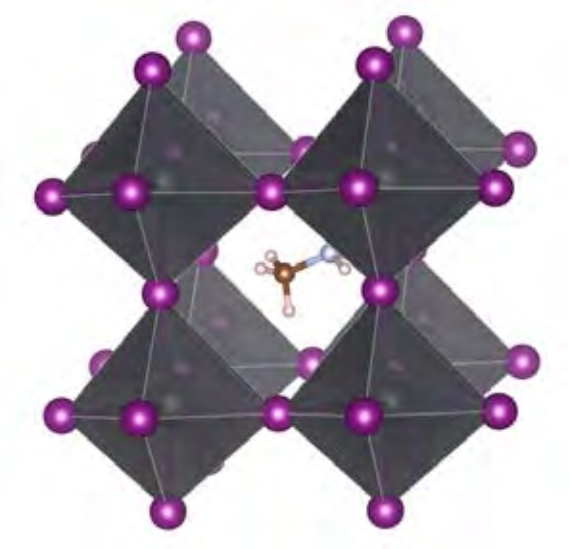

Figure A.1: Atomic position of Phase I of $MAPbI_3$.

Cell Parameters (in Å)

Cell Parameters	X	Y	Z
a	6.3172799721	0	0
b	0	6.3172799721	0
c	0	0	6.3172799721

Atomic Position (in fractional coordinates)

Atomic Position	X	Y	Z
C	0.893988013	0.999817014	0.457830995
N	0.109073997	0.000006974	0.547769010
H	0.910149992	0.999642015	0.285777003
H	0.808676004	0.144703984	0.511030972
H	0.808885992	0.854951978	0.511300981
H	0.196268976	0.135748982	0.501513004
H	0.196411014	0.864210010	0.501782000
H	0.106339991	0.000186980	0.711217999
Pb	0.444884002	0.499979973	0.977622986
I	0.409487009	0.499981999	0.475145012
I	0.399271011	0.999958038	0.023664000
I	0.932343006	0.499994993	0.922478974

Table A.2: Input atomic position of cubic $MAPbI_3$ for *fix:cell*

Cell Parameters (in Å)

Cell Parameters	X	Y	Z
a	6.3172799721	0	0
b	0	6.3172799721	0
c	0	0	6.3172799721

Atomic Position (in fractional coordinates)

Atomic Position	X	Y	Z
C	0.893988013	0.999817014	0.457830995
N	0.109073997	0.000006974	0.547769010
H	0.909106650	0.028665029	0.288037806
H	0.799048099	0.128081848	0.532579746
H	0.819553197	0.842694770	0.487500089
H	0.186278327	0.147115831	0.523804623
H	0.205440005	0.879661112	0.481574022
H	0.107299788	0.973471875	0.709138268
Pb	0.500000000	0.500000000	1.000000000
I	0.500000000	0.500000000	0.500000000
I	0.500000000	1.000000000	0.000000000
I	1.000000000	0.500000000	1.000000000

Table A.3: Input atomic position of cubic $MAPbI_3$ for *fix:cell+PbI$_3$*

APPENDIX B

THE VAN DER WAALS INTERACTION CONFIGURATION IN QUANTUM ESPRESSO

Documented in Quantum Espresso 5.4.0 as follows:

'dft' is the exchange-correlation functional label, described either by short names listed below, or by a series of keywords (everything is case-insensitive). 'dft_shortname' contains one of the short names listed below (deduced from from 'dft' as read from input or PP files)

- 'pbesol'= 'sla+pw+psx+psc' = PBEsol
- 'vdw-df' ='sla+pw+rpb +vdw1' = vdW-DF1
- 'vdw-df2' ='sla+pw+rw86+vdw2' = vdW-DF2
- 'vdw-df-c09' ='sla+pw+c09x+vdw1' = vdW-DF-C09
- 'vdw-df2-c09' ='sla+pw+c09x+vdw2' = vdW-DF2-C09
- 'vdw-df-cx' ='sla+pw+cx13+vdW1' = vdW-DF-cx
- 'vdw-df-obk8' ='sla+pw+obk8+vdw1' = vdW-DF-obk8 (optB88-vdW)
- 'vdw-df-ob86' ='sla+pw+ob86+vdw1' = vdW-DF-ob86 (optB86b-vdW)
- 'vdw-df2-b86r' ='sla+pw+b86r+vdw2' = vdW-DF2-B86R (rev-vdw-df2)
- 'rvv10' = 'sla+pw+rw86+pbc+vv10' = rVV10

Any nonconflicting combination of the following keywords is acceptable:

References:

pz J.P.Perdew and A.Zunger, PRB 23, 5048 (1981)

vwn S.H.Vosko, L.Wilk, M.Nusair, Can.J.Phys. 58,1200(1980)

wig E.P.Wigner, Trans. Faraday Soc. 34, 67 (1938)

hl L.Hedin and B.I.Lundqvist, J. Phys. C4, 2064 (1971)

gl O.Gunnarsson and B.I.Lundqvist, PRB 13, 4274 (1976)

pw J.P.Perdew and Y.Wang, PRB 45, 13244 (1992)

obpz G.Ortiz and P.Ballone, PRB 50, 1391 (1994)

obpw as above

b88 A.D.Becke, PRA 38, 3098 (1988)

p86 J.P.Perdew, PRB 33, 8822 (1986)

pw86 J.P.Perdew, PRB 33, 8800 (1986)

b86b A.D.Becke, J.Chem.Phys. 85, 7184 (1986)

ob86 Klimes, Bowler, Michaelides, PRB 83, 195131 (2011)

b86r I. Hamada, Phys. Rev. B 89, 121103(R) (2014)

pbe J.P.Perdew, K.Burke, M.Ernzerhof, PRL 77, 3865 (1996)

pw91 J.P.Perdew and Y. Wang, PRB 46, 6671 (1992)

blyp C.Lee, W.Yang, R.G.Parr, PRB 37, 785 (1988)

hcth Handy et al, JCP 109, 6264 (1998)

olyp Handy et al, JCP 116, 5411 (2002)

revPBE Zhang and Yang, PRL 80, 890 (1998)

pbesol J.P. Perdew et al., PRL 100, 136406 (2008)

q2d L. Chiodo et al., PRL 108, 126402 (2012)

rw86 E. Amonn D. Murray et al, J. Chem. Theory comp. 5, 2754 (2009)

wc Z. Wu and R. E. Cohen, PRB 73, 235116 (2006)

kzk H.Kwee, S. Zhang, H. Krakauer, PRL 100, 126404 (2008)

pbe0 J.P.Perdew, M. Ernzerhof, K.Burke, JCP 105, 9982 (1996)

hse Heyd, Scuseria, Ernzerhof, J. Chem. Phys. 118, 8207 (2003)

Heyd, Scuseria, Ernzerhof, J. Chem. Phys. 124, 219906 (2006).

b3lyp P.J. Stephens,F.J. Devlin,C.F. Chabalowski,M.J. Frisch

J.Phys.Chem 98, 11623 (1994)

vdW-DF M. Dion et al., PRL 92, 246401 (2004)

T. Thonhauser et al., PRL 115, 136402 (2015)

vdW-DF2 Lee et al., Phys. Rev. B 82, 081101 (2010)

rev-vdW-DF2 I. Hamada, Phys. Rev. B 89, 121103(R) (2014)

vdW-DF-cx K. Berland and P. Hyldgaard, PRB 89, 035412 (2014)

vdW-DF-obk8 Klimes et al, J. Phys. Cond. Matter, 22, 022201 (2010)

vdW-DF-ob86 Klimes et al, Phys. Rev. B, 83, 195131 (2011)

APPENDIX C

ADDITIONAL AMBIENT PRESSURE SIMULATION RESULTS

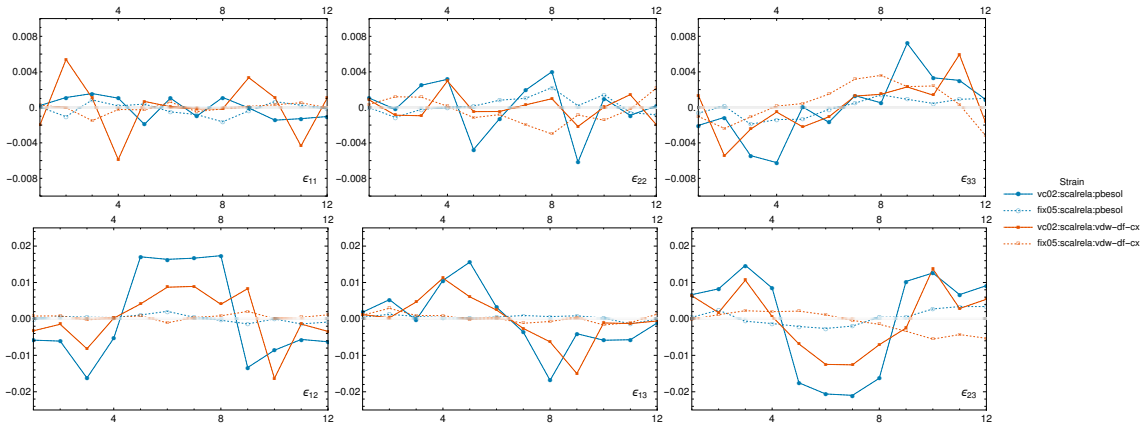

Figure C.1: Strain of the simulation cell in *relax*

APPENDIX D

EXTENDED ACKNOWLEDGEMENTS

The regulation limits the front acknowledgement section not to be longer than one page. However, so many people had joined me in this story that I would regret if I cannot express my gratitude to them. Therefore, I would like to use this space to acknowledge them.

Had it not been for Dr. Puchong Laurujisawat's continual support and sympathy, I would have been long lost. I am touched by the length and breadth he fared to help me out.

I could not have finished this thesis without the support of the people around me. These indispensable 'friendship' had guided me through the darkest abyss I walked through for the most of this journey. I would have given up both science and life altogether without these people. They are not just important, but indeed indispensable pieces of the story. I thanked Mr. Tiraput Poonpanichkul and Mr. Sangrag Cholsaranon for their company, for that life would be monotonous without them. I thanked Mr. Theerapat Tansuwannont for offering numerous assistance and accompaniment even when we are literally half the globe apart. There's also Mr. Ittipat Promnorakid who came to the rescue at critical moments, and Mr. Teerapat Payupol who rendered late-at-night lab stays much less lonely. Also, Miss Chamaphan Khanachaiwiruj, Miss Yanin Thipakorn, Miss Wiphada Det-amnatkul, Miss Jidapa Ammaritchatchawal and Miss Grittigar Sangasang whom we only occasionally see each other, but meeting up with them had me filled up on joy to the brim.

This thesis is a solid proof that, for once, I did not give up on myself, and that I am never been truly abandoned.

Biography

Vichawan Sakulsupich is a curious person who enjoys learning new problem-solving techniques. Born on August 3rd, 1991. Her main interest lies in the field of condensed matter physics, fluid dynamics and meteorology.

Education background:

2014 Bachelor of Science (Physics), Chulalongkorn University, Thailand

2011 Scienc-majored Secondary Education, Triam Udom Suksa School, Thailand

Academic activities:

2017 Structural dynamics with respect to on-axis CH_3NH_3 rotation in $CH_3NH_3PbI_3$ hybrid organic – inorganic perovskites: semi-local versus non-local density functional based calculations.

2017 Model of High Pressure Phase IV and V of $MAPbI_3$ Perovskite

2017 Oral presentation in Siam Physics Congress 2017

2016 Grantee of 90^{th} Anniversary of Chulalongkorn University Scholarship

2016 Oral Presentation in Siam Physics Congress 2016

2013 Grantee of Development and Promotion of Science and Technology Talents Project (DPST)